

PROCESSING AND TOPOTHERMAL CONVERSION OF
MANGANESE OXIDE NANOASSEMBLIES

BY

TREVYN A. HEY

A THESIS
SUBMITTED TO THE FACULTY OF

ALFRED UNIVERSITY

IN PARTIAL FULFILLMENT OF THE REQUIREMENTS
FOR THE DEGREE OF

MASTER OF SCIENCE

IN

MATERIALS SCIENCE AND ENGINEERING

ALFRED, NEW YORK

FEBRUARY, 2017

PROCESSING AND TOPOTHERMAL CONVERSION OF
MANGANESE OXIDE NANOASSEMBLIES

BY

TREVYN A. HEY

B.S. CLEMSON UNIVERSITY (2013)

SIGNATURE OF AUTHOR _____

APPROVED BY _____

SCOTT T. MISTURE, ADVISOR

STEVEN M. PILGRIM, ADVISORY COMMITTEE

DAVID W. LIPKE, ADVISORY COMMITTEE

CHAIR, ORAL THESIS DEFENSE

ACCEPTED BY _____

ALASTAIR N. CORMACK, INTERIM DEAN
KAZUO INAMORI SCHOOL OF ENGINEERING

Alfred University theses are copyright protected and may be used for education or personal research only. Reproduction or distribution in part or whole is prohibited without written permission from the author.

Signature page may be viewed at Scholes Library, New York State College of Ceramics, Alfred University, Alfred, New York.

ACKNOWLEDGMENTS

This work is the result of several years of research that have taken me around the globe. I had the opportunity to travel to Japan and live there for three months, doing research at a national lab under an excellent researcher working with fantastic students from around the world. My experiences abroad have only served to highlight the quality of the faculty, facilities, and students here at Alfred. Working with nanomaterials is no easy feat, and it was challenging never knowing for sure if one experiment would perform the same as the last, but with the support of everyone here I was able to make it through.

First of all, I have to thank my advisor, Dr. Scott Misture, for inviting a polymer chemistry student in to begin working on ceramics. If not for him, I wouldn't have been here at all. Secondly, I want to thank the members of my committee, Dr. Steve Pilgrim and Dr. David Lipke, for their help and advice both towards this work and my academic career in general.

My whole family deserves a note for the sheer amount of encouragement they have shown me as I pursued my studies, both as an undergrad and a graduate student.

The life of a grad student is not something many can relate to, so having a community of other students to use as support was invaluable. The list is too long to write properly, but I want to thank Victoria Blair, Peter Metz, Fiona Cormack, Kyle McDevitt, Peter Sowinski, and Tyler Gubb for the time they have taken to help me get along in Alfred in and out of the lab. Skylar Johnson, of Washington State University, was my lifeline in Japan and has since become my biggest cross-country supporter.

Working inside the lab would be too much without some external outlet, so I'll be forever grateful to Shihan Elise Flynn and the community at Alfred Martial Arts for helping me blow off some steam and introducing me to some very kind and very scary friends. The entire Norris family deserves my endless thanks for accepting me into their home and treating me as a member of the family. Nothing is better for a starving grad student than a home-cooked meal and some pleasant company. People always seem to end up back in Alfred for one reason or another, and I know I've found mine.

TABLE OF CONTENTS

	Page
Acknowledgments	iii
Table of Contents	iv
List of Tables	vi
List of Figures	vii
Abstract	ix
I INTRODUCTION.....	1
A. Background on Layered Materials.....	1
B. Applications for Energy Storage	4
C. MnO ₂ as an Earth-abundant, Non-toxic, and Easily Processed Material	5
D. Polymorphs of MnO ₂	6
E. Behavior of δ -MnO ₂	7
F. Applications of MnO ₂	10
1. Photocatalytic Activity	10
2. Electrochemistry	10
3. Sorbents and Filters	10
G. Phase Evolution in MnO ₂	10
II EXPERIMENTAL PROCEDURE.....	12
A. Powder Synthesis.....	12
B. Ion Exchange	12
C. Exfoliation	13
D. Flocculation	13
E. X-ray Diffraction	13
F. Scanning Electron Microscopy.....	14
G. Thermogravimetric Analysis	14
H. Surface Area Measurement.....	14
I. Electrochemical Measurement.....	15
III RESULTS AND DISCUSSION.....	16
A. Synthesis.....	16
B. Ion Exchange	23
C. Exfoliation	25

D. Flocculation	28
E. Defects in MnO ₂ Nanosheets.....	31
F. Electrochemical Performance and the Role of Defects	32
G. High-Temperature Phase Stability and Phase Transitions to Form Tunnel-structured α -MnO ₂	32
1. Parent phase	33
2. Ion-exchanged phase	34
3. Flocculated material.....	35
H. Mechanism of Phase Transformations.....	39
IV SUMMARY AND CONCLUSIONS.....	40
V FUTURE WORK	41
REFERENCES.....	42

LIST OF TABLES

	Page
Table I. XRF Potassium Content Analysis	23
Table II. Cation Ion Exchange Analysis	24
Table III. Cations Exchanged and Phase Composition After 800 °C Treatment	34

LIST OF FIGURES

	Page
Figure 1. KTiNbO ₅ with sheets comprised of two octahedra.....	2
Figure 2. BCNN layered perovskite with intermediate Bi ₂ O ₂ ⁻ layer (n=3). ⁶	3
Figure 3. Lithium-ion battery working diagram. ¹⁷	4
Figure 4. Polymorphs of MnO ₂ , showing (a) α- (cryptomelane), (b) β- (pyrolusite), (c) γ- (intergrowth of ramsdellite/pyrolusite), and (d) δ- (birnessite) MnO ₂ . ¹⁸	7
Figure 5. Structure of the birnessite MnO ₂ sheet (left) with out-of plane defects (right). ³¹	8
Figure 6. Parent-phase K _{0.45} MnO ₂ prepared by solid-state synthesis showing faceting and hexagonal symmetry.	17
Figure 7. Hydrothermally-grown δ-MnO ₂ nanoflowers and α-MnO ₂ nanowires.	17
Figure 8. XRD of birnessite synthesized by solid-state (black), hydrothermal (red) and aqueous precipitation (blue) methods.	18
Figure 9. HTXRD of parent phase birnessite in air.	20
Figure 10. XRD of the K _x MnO ₂ 001 peak for x=0.35 (black), 0.40 (red), 0.45 (blue), 0.50 (green), 0.55 (pink), and 0.60 (brown).....	20
Figure 11. Mass loss on heating parent phase birnessite in air at 20 K/min.	21
Figure 12. XRD of K _{0.40} Na _{0.05} MnO ₂ showing growth of α-MnO ₂ (▲) and δ-MnO ₂ (●).	22
Figure 13. K _{0.40} Na _{0.05} MnO ₂ microstructure with regions of tube-like α-MnO ₂ and plate-like δ-MnO ₂	22
Figure 14. Parent-phase birnessite (black, bottom) substituted with copper (blue, top) and iron (red, middle) on a square-root scale.	23

Figure 15. Shift in basal peaks from the parent-phase (black) to the proton-exchanged phase (red).....	24
Figure 16. Unexfoliated powder remaining after centrifugation of nanosheets (black) with the proton-exchanged pattern (red) overlaid showing a pillared phase (*). ...	26
Figure 17. Flocculated nanosheets exfoliated via (left) orbital mixer and (right) ultrasonic bath dried from isopropanol.....	27
Figure 18. AFM of MnO ₂ nanosheets with a thickness of 3.8 nm.	27
Figure 19. Dried nanosheet suspension showing restacked 00l peaks.	28
Figure 20. BET of MnO ₂ nanosheets flocculated at pH 2 using HCl. SSA=94 m ² /g.	29
Figure 21. Nanosheets flocculated with HCl at pH 2, dried from an aqueous suspension at 60 °C.	30
Figure 22. PDF analysis of MnO ₂ defects as a function of processing. ⁶¹	32
Figure 23. HTXRD of parent-phase birnessite (●) washed in water showing growth of α-MnO ₂ (▲).	33
Figure 24. Growth of α-MnO ₂ from Na _{0.03} MnO ₂ as seen in HTXRD.....	34
Figure 25. Microstructural evolution of MnO ₂ floccules heated in air.	36
Figure 26. PDF data of H-flocculated MnO ₂ (blue) with a cryptomelane structure fit (red), by Peter Metz.	37
Figure 27. MnO ₂ nanosheets flocculated with NaCl, heated to 800 °C in air showing Mn ₂ O ₃ (●) and tunnel-structured Na ₄ Mn ₉ O ₁₈ (▲).	38
Figure 28. Growth of α-MnO ₂ in an Mn ₂ O ₃ matrix from Na-flocculated nanosheets shown before and after heat treatment at 800 °C for 12 hours.	38
Figure 29. Linking of out-of-plane MnO ₆ octahedra to form tunnels. ⁶³	39

ABSTRACT

Layered oxides offer a promising approach to creating nanostructured materials through exfoliation of parent crystals into single nanosheet layers. These nanosheets, which are only atoms thick but microns wide, present unique opportunities for microstructure control not available with conventional nanoparticles or nanotubes. Flocculation of exfoliated nanosheets provides an easy route to highly porous solids without further processing, which makes it possible to produce materials for catalysts, active electrodes, and other applications that benefit from macro- and mesopores and high surface area.

In this work, birnessite, a layered polymorph of MnO_2 , was synthesized using solid-state and hydrothermal techniques. The high-temperature stability and microstructure evolution was studied in ion-exchanged and flocculated samples. Through controlled processing, it is possible to encourage the growth of a small amount of tunnel-structured $\alpha\text{-MnO}_2$ along with Mn_2O_3 . While the thin nanosheets disappear with heat treatment, the high surface area of the starting porous solid is maintained. Through surface-tension effects, the sheets transform into nodules in an open network that mimics a spinodally-decomposed solid, where Mn_2O_3 forms an interconnected solid structure in air.

High-energy x-ray diffraction (HEXRD) was used to observe defects in nanosheets created during processing, and track changes with heat treatment. It was found that these defects play a role in the high-temperature phase stability. At temperatures as low as 200 °C, HEXRD revealed the presence of tunnel-structured MnO_2 , caused by the migration of surface Frenkel defects in the form of MnO_6 octahedra on the surface of the sheets. Without a stabilizing cation, as the temperature increases to 600 °C, Mn_2O_3 begins to form. However, if a cation such as Na^+ is introduced through ion exchange or via flocculation, $\alpha\text{-MnO}_2$ is stable to at least 800 °C.

The low-temperature conversion of $\delta\text{-MnO}_2$ nanosheet floccules to $\alpha\text{-MnO}_2$ yielding a porous network of nanosheets offers exciting opportunities in electrochemistry and colloidal chemistry with numerous applications.

INTRODUCTION

A. Background on Layered Materials

Layered materials have garnered interest lately due to the unique processing approaches and applications enabled by their two-dimensional nano-scale structure. The most well-known example of a layered compound in popular science today is graphite, which can be delaminated into graphene sheets and is commonly extolled to the public due to the numerous applications researchers have discovered.¹ While graphene is unique among layered compounds due to the hybridized bonding exhibited by carbon, many of the exciting and innovative processing techniques and applications can be transferred to ceramic analogues that are more chemically robust and compositionally flexible.²

Layered oxide materials can form from a wide range of starting chemistries, and this chemistry can be tailored to tune the material properties to specific applications. Many of these layered oxides consist of strongly bound two-dimensional sheets separated by weakly bound ionic layers. Others consist of sheets bound together covalently by an intermediate oxide layer. Through a combination of chemical and mechanical means, these sheets can be separated, cleaving the ionically bound layer or removing the intermediate oxide, resulting in suspensions of free-floating nanosheets with charged surfaces. Nanosheet suspensions can be used directly, or can be processed to form, for example, thin films via Langmuir-Blodgett or electrophoretic deposition, or open-network structures via flocculation.³

Ceramics have long been in use due to the abundance of starting materials that naturally occur on earth and the ease of production requiring only a heat source for firing. Recently, advanced ceramics have been developed with carefully controlled synthesis and processing methods to achieve desired microstructures and properties, but this often requires the use of expensive or hazardous materials or techniques. By manipulating the size scale, nanosheets can be used to tune resultant macroscopic properties in a way that is not possible with bulk processing methods. Nanosheet systems frequently are composed of simple chemistries, and instead derive their interesting properties from their

nanoscale morphology. While most ceramic nanosheets are not as thin as graphene sheets (which can be merely 1 carbon atom thick), they still are well within the lengthscale of nanomaterials, with systems on the thicker side being comprised of layers only tens of atoms thick. Many systems are much thinner than that, and are often a single octahedron thick – only three atoms from one face to the other.

The most common atomic arrangement for layered compounds is that of stacks of octahedral layers. Transition metal cations often coordinate with oxygen to form MO_6 units that take the shape of octahedra. These octahedral units can be connected in a number of ways, including corner-sharing, edge-sharing, and face-sharing configurations. The combination of these different connections can create sheets with unusual and interesting structures that might be leveraged in various applications.

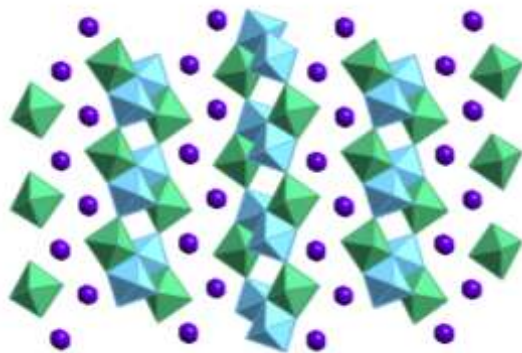


Figure 1. KTiNbO_5 with sheets comprised of two octahedra

There is a series of titanoniobate oxides that have different size steps in the sheet due to differing connections between the octahedra. The combination of edge-sharing and corner-sharing octahedra creates a tiered sheet surface with different step lengths. For example, Figure 1 shows KTiNbO_5 , a titanoniobate with steps comprised of 2 octahedra, with adjacent sheets offset to allow for closer stacking.⁴ Some work has been done with the exfoliation and flocculation of these sheets in order to determine if the slight difference in chemistry or sheet morphology results in any changes in photocatalytic or electrochemical performance.⁵ For example, sheets with shorter steps may have a higher density of active sites for catalytic reactions if the step edge behaves differently than the middle of the step.

Much work has also been done on Aurivillius-phase oxides with the composition $\text{Bi}_2\text{A}_{n-1}\text{B}_n\text{O}_{3n+3}$ (BCNN) where the sheet thickness can be tailored from $n=2$ to 5 and possibly beyond, where n is the number of octahedra from face to face of the sheet. Blair, et al., have tracked the change in photocatalytic activity with sheet thickness in these materials.⁶ Figure 2 shows the crystal structure for an $n=3$ BCNN. Other properties, such as ferroelectricity from distorted octahedra, can arise from the structural relaxation of these sheets of different thicknesses. In nanosheets, these inherently become nano-domained materials.

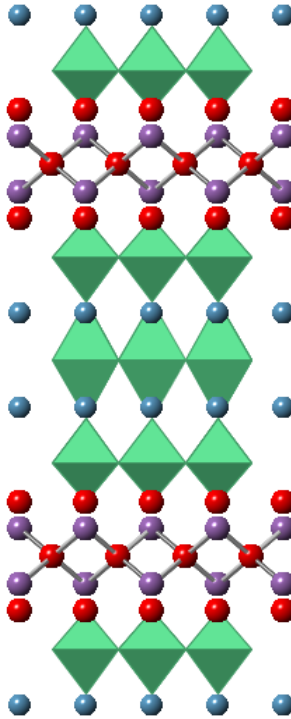


Figure 2. BCNN layered perovskite with intermediate Bi_2O_2^- layer ($n=3$).⁶

Another well-studied nanosheet system is that of TiO_2 . Sasaki, et al., have created a significant body of work using exfoliated Li_xTiO_2 .⁷⁻⁹ By layering TiO_2 nanosheets in homogeneous films or heterogeneous films with other nanosheet systems, Sasaki's group was able to create films with diverse properties for uses such as dielectrics and spinelectronics, and for use in epitaxial growth.^{3,10-15}

B. Applications for Energy Storage

With the recent global push for clean energy and the constant demand for higher-capacity and faster-charging electronic devices, improving charge storage technology has come to the forefront in public demand for research. A report from the Department of Energy stated that over \$1.3 billion was invested in energy storage research between 2009 and 2012 by a number of government agencies.¹⁶ With recent investments such as Elon Musk's Powerwall™ technology as part of his company Tesla, energy storage has gotten cheaper and more readily available. However, in order to fully utilize all of the available renewable energy sources available to us such as solar and wind power, energy storage must continue to improve.

Lithium ion batteries (Figure 3) are still plagued with a number of issues, including limited cyclability and the scarcity of the requisite materials, particularly lithium. They also come with a host of hazards, such as the potential to catch fire should the housing be breached. Nowadays, nearly every consumer electronic comes equipped with a permanent or long-term rechargeable battery, and it is in everyone's interest to make sure that they are as safe as possible. In 2016, Samsung, a major cell phone producer, had to recall every Galaxy Note 7 they produced due to issues that caused the batteries to overheat and explode.

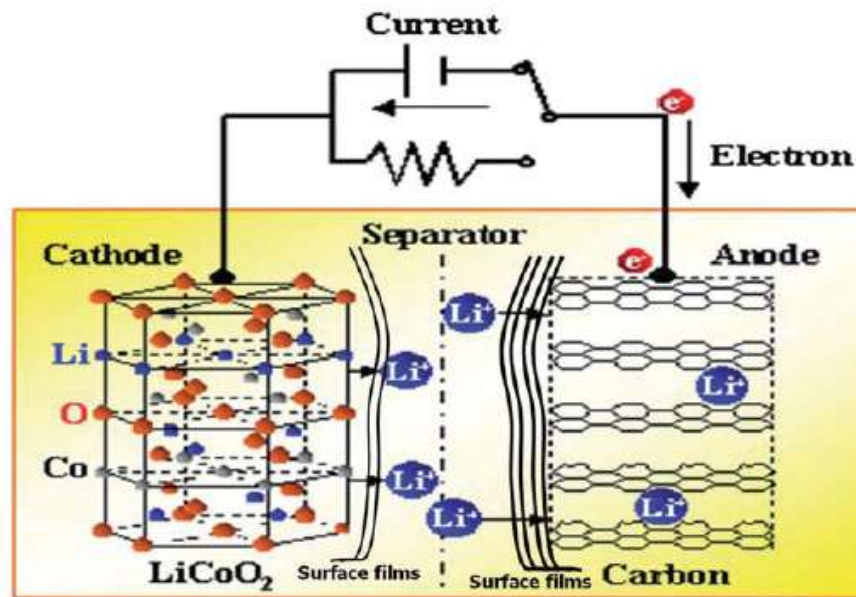


Figure 3. Lithium-ion battery working diagram.¹⁷

Cyclability is a concern for many rechargeable energy storage solutions, since most commonly the mechanism for charge storage requires the intercalation of ions – typically small alkali ions such as Li^+ and Na^+ – into a crystalline lattice. A lattice can only accommodate so many ions intercalated into its structure before the strain on the lattice causes defects to form in the crystal. When enough defects form, the battery material breaks and becomes unusable. The cations can also become irreversibly intercalated and trapped in the lattice, meaning they are no longer available to participate in the charge transfer process. In both cases, the overall charge storage capacity will be drastically reduced. The intercalation process is also time dependent, and for large batteries it can take hours to charge and discharge. The burgeoning area of nanoscience has opened up many new avenues to approach conventional problems in electronics, and more specifically, in charge storage. There are many benefits to investigating new solutions to old issues, including lowered cost, improved efficiency, and reduced size. Lowering the price and size, and improving efficacy of parts for consumer electronics could have wide-reaching effects.

The concerns about rechargeable batteries indicate that there is opportunity for a new type of charge storage – one that is made from readily available (Earth-abundant) materials that can charge quickly, and have high charge storage capabilities. Nanosheets based on manganese have a number of advantages. First, manganese is Earth-abundant and non-toxic, meaning that parts can more readily be made economically and safely. Second, the ease of making nanostructured materials makes processing scalable. Third, the high surface area of nanosheets has beneficial impacts on the size and weight of components manufactured using these materials. Manganese oxides suit this purpose admirably due to the high concentration of Mn compounds in the Earth's crust, the variable valence states of Mn (2+, 3+, 4+, 7+) with the accompanying chemistry opportunities, and the readiness of Mn to form layered compounds.

C. MnO_2 as an Earth-abundant, Non-toxic, and Easily Processed Material

One of the strongest arguments for the use of transition metal oxides in batteries, capacitors, and catalysts is their relative abundance on Earth. The most effective lab-scale

catalysts are commonly rare earth-based or rely on noble metals which are often not scalable to industrial level production due to cost. If new advanced materials can be discovered that have similar performance to the expensive rare-earth or noble metal options, the price of current battery materials will quickly cause them to be replaced by the more economical transition metal oxide option.

Another concern with current products is that they rely on heavy metal elements such as bismuth, lead, and antimony. This creates problems if the part were to fail and expose consumers to toxic compounds that could lead to health problems. Additionally, disposal becomes much more challenging to prevent the heavy metals from leaching into the ground. Using manganese as the active material avoids these problems due to manganese's non-toxicity.

Manganese oxides are easily processed powders, not requiring controlled atmospheres or specialized furnaces. Layered and tunneled polymorphs form from uncomplicated processes that can be scaled up to result in high yields without compromising phase purity. This contrasts with some current materials, such as carbon nanotubes or single crystal silicon, which are time-consuming and difficult to produce in large quantities.

D. Polymorphs of MnO₂

MnO₂ can form several different polymorphs, including α -, β -, γ -, δ -, and R-MnO₂. While they are all distinct, they differ only slightly. The difference, though small, has large repercussions on the processing and applications that apply to each polymorph. The α -, β -, and γ -MnO₂ polymorphs have 1-dimensional tunnels with different tunnel side lengths, as shown in Figure 4. Here, α -MnO₂ (cryptomelane) consists of 2x2 tunnels, while β -MnO₂ (pyrolusite) has 1x1 tunnels, and γ -MnO₂ has alternating 1x1 and 1x2 tunnels. R-MnO₂ (ramsdellite) has 1x2 tunnels. The δ - phase (birnessite) has layers of MnO₆ octahedra that are not linked between the layers.¹⁸

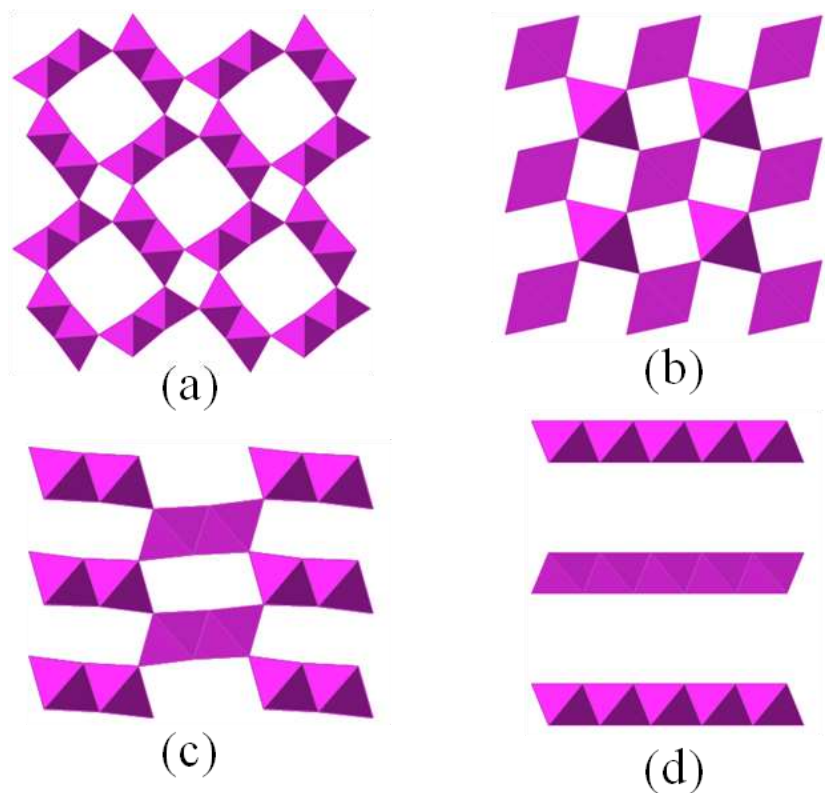


Figure 4. Polymorphs of MnO_2 , showing (a) α - (cryptomelane), (b) β - (pyrolusite), (c) γ - (intergrowth of ramsdellite/pyrolusite), and (d) δ - (birnessite) MnO_2 .

Tunnel-structured materials are of interest for many applications due to their one-dimensional diffusion pathways. The δ - MnO_2 polymorph is a naturally-occurring layered material, in which sheets of edge-sharing octahedra form planes separated by an interlayer cation. The nature of the interlayer cation is variable, and studies have been conducted investigating the effect of the interlayer cation on bulk material properties. The dimensions of the crystals can be affected by the processing techniques used. Groups have reported forming sheets¹⁹⁻²³ (roughly the same length in-plane) and belts²⁴⁻²⁶ (long in one direction and narrow in the other).

E. Behavior of δ - MnO_2

There has been a large amount of high-quality research done with layered manganese oxides due to their prevalence on the ocean floor. They serve an important role in ion regulation and have therefore received much attention from geologists and

marine biologists.^{27,28} The common forms of MnO_2 on the ocean floor are birnessite, buserite, and todorokite. Birnessite and buserite are layered compounds comprised of MnO_2 sheets, with buserite having an extra hydration layer and thus an expanded interlayer compared to birnessite. Todorokite is a hydrated structure containing 3x3 tunnels. Each of these structures have layer/tunnel alkali ions such as Na^+ , K^+ , and Ca^{2+} .^{27,29}

There are a number of documented procedures for synthesizing birnessite. For geologic surveys, birnessite is synthesized through hydrothermal or aqueous precipitation methods, which forms compounds similar to those formed in nature. For other studies, birnessite has been synthesized via solid-state processes.^{19,30}

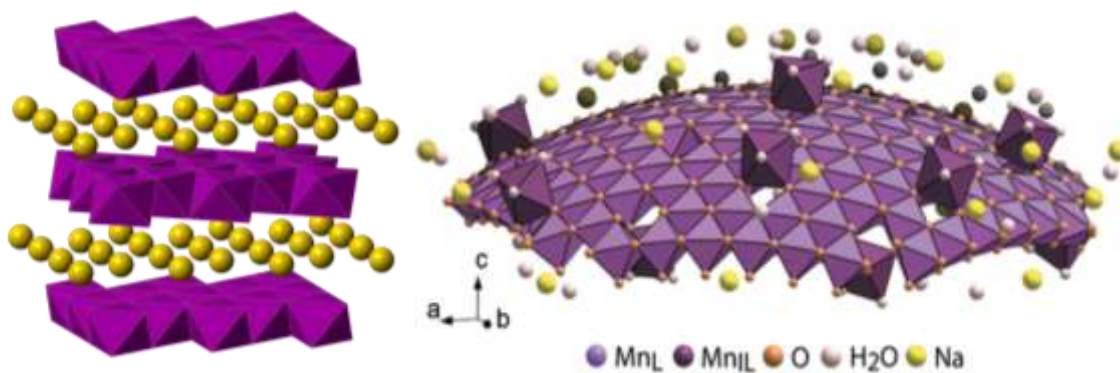


Figure 5. Structure of the birnessite MnO_2 sheet (left) with out-of plane defects (right).³¹

The structure of the sheet (Figure 5) is largely composed of in-plane MnO_6 octahedra, but under various conditions, some of the Mn can be reduced from 4+ to 3+, which causes a distortion of the octahedron and strains the network. This distortion, termed the Jahn-Teller effect, has been observed in other systems containing Mn^{3+} octahedra, such as Mn_2O_3 .³² To relieve the in-plane strain, the octahedra can move to a surface position as seen in Figure 5. Work has been done to model this and track the effects of these sheet defects on electrochemical properties, and determined that there is a positive trend with these defects and charge capacity.³¹

The potassium ions in the interlayer of highly-crystalline $\delta\text{-MnO}_2$ synthesized via solid-state methods are still mobile species. By introducing a strong enough chemical

potential gradient, it is possible to encourage the exchange of K^+ in the interlayer with other cationic species in an aqueous suspension.²⁹

Adding powders to 1 M solutions of chloride salts allows the K^+ in the parent phase to exchange with the cations in solution. Thus, treating with 1 M HCl exchanges the potassium in the interlayer with H^+ and H_2O .³³

It is also possible to exchange the K^+ (or H^+ in proton-exchanged samples) with other cations, including Li^+ , Na^+ , and Ca^{2+} . It has been shown that introducing different cations into the interlayer of aqueously prepared birnessites changes the hydration energy of water in the interlayer, and can change the band gap and electrical properties of the material.^{33,34} Much work has been done on these systems using hydrothermal or aqueous-precipitated birnessite,²⁹ but there is only limited work on samples exchanged from solid-state precursors.³⁵ The present work focuses on the ion-exchange of solid-state-synthesized birnessite using conditions similar to those reported for hydrothermal and aqueous samples in literature. Birnessite synthesized through solid-state techniques with potassium as the layering cation has been shown to be stable at temperatures as high as 900 °C, but hydrothermally prepared samples and samples prepared with other layering cations have not shown stability above 200-300 °C.²⁹ They commonly transform into tunnel-structured α - MnO_2 ,²⁹ spinels (in the case of Li ^{36,37}), Mn_2O_3 ,^{38,39} and Mn_3O_4 .⁴⁰

The addition of tetrabutylammonium hydroxide (TBA-OH) causes swelling and delamination of the Mn-based nanosheets. This is aided by the expanded interlayer that results from treating the sample with HCl and is thus performed on ion-exchanged samples.⁴¹⁻⁴³ In water, the molecule disassociates into TBA^+ and OH^- . The bulky TBA^+ inserts itself between the sheets and associates with the negatively-charged sheet surface, expanding the interlayer and causing them to exfoliate and become suspended in the aqueous solution. Other bulky organic groups have been shown to produce similar results.⁴⁴

Suspensions of exfoliated nanosheets are stable over some months, but it is possible to destabilize them through the addition of ionic species such as protons or alkali.^{5,45,46} Such flocculated samples form monoliths exhibiting high surface area and porosity, with specific surface area typically between 100 and 200 m^2/g .

F. Applications of MnO₂

Due to its prevalence in nature, MnO₂ has been used for various purposes to serve as a synthetic analogue for natural processes.

1. Photocatalytic Activity

Manganese serves as the central ion in the metal complex responsible for photosynthesis in plants. Thus, it has garnered interest as a photocatalyst and work has been done to use manganese oxides for water oxidation and gas catalyst reactions.^{34,47-49}

2. Electrochemistry

Due to the variable valence state of manganese, which can exist as Mn 2+, 3+, 4+, and 7+, it has been heavily investigated as the active material in electrochemical capacitors. A number of groups have reported specific capacitance values between 200 and 300 F/g^{50,51} and even as high as 600 F/g in one case.⁵² Often, these electrodes take advantage of the high surface area of MnO₂ nanostructures and make use of composites and binders.

3. Sorbents and Filters

Due to its natural nanostructure and affinity to cations, manganese compounds have been used as filters, molecular sieves, and absorbents. They can regulate ions in marine environments, and find uses as sorbents for heavy metal ions such as radium.^{27,53,54}

G. Phase Evolution in MnO₂

By introducing defects into the sheet structure either during synthesis or via processing methods, the sheet becomes thermodynamically unstable and a phase change occurs upon heating. In hydrothermally- and aqueously-grown δ -MnO₂ it is reported that the sheet structure is stable only to approximately 200 °C.^{29,33,55} In these defective sheets, the reported transformation is that of the layered structure to a tunnel-structured material, commonly α -MnO₂, cryptomelane. Birnessite synthesized via high-temperature methods are stable without further processing, and little work has been done to characterize the effect of defects on the high-temperature phase stability in these materials.

This work investigates the role of processing on phase and microstructure evolution in high-quality birnessite, synthesized via solid-state methods. By introducing defects and modifying the interlayer gallery, the phase stability was tracked up to 800 °C. Flocculating exfoliated nanosheets provides a route to high-specific-surface-area, porous solids. The microstructures of these floccules were likewise tracked throughout the processing steps to determine if these porous solids are stable.

EXPERIMENTAL PROCEDURE

A. Powder Synthesis

Birnessite (δ -MnO₂) was synthesized by calcining mixed powders of MnCO₃ and K₂CO₃ in a molar ratio of 40:9. Approximately 5 grams of powders were mixed using a McCrone micronising mill using 30 ml of isopropanol and alumina media for 5 minutes. The mixed powders were dried on a hot plate for 30 minutes over low heat. The dried powder was collected and heated to 900 °C in air at a rate of 5 K/min in an uncovered alumina crucible without a powder bed for 12 hours to form the compound K_{0.45}MnO₂. This δ -MnO₂ “parent phase” was characterized by XRD to confirm phase purity.

B. Ion Exchange

To remove the potassium, 0.5 g of the parent phase was added to 50 ml of 1 normal HCl in a plastic centrifuge tube and placed in a Branston 1510 ultrasonic bath for 4 hours, manually shaking every 30 minutes to redisperse the powders. After 4 hours, the powder was collected by centrifugation at 3500 rpm, and the acid was decanted. The powder was added to fresh 1 N HCl and placed in the ultrasonic bath for an additional 4 hours. This two-step process was repeated a total of 3 times to encourage complete potassium exchange. After the third ion-exchange, the powders were washed to neutral pH using deionized (DI) water, and dried in an oven at 60 °C. The extent of the ion-exchange was tracked using EDS and XRD.

Bulk-phase ion-exchanged powders were produced by adding the parent phase or proton-exchanged phase powder to a 1 M solution containing the desired exchange cation. Cations used for this exchange included Li⁺, Na⁺, K⁺, Cs⁺, Mg⁺, Sr²⁺, and Zn²⁺. For this, 0.5 g of the initial powder was added to 50 ml of 1 M solution and allowed to exchange in the ultrasonic bath for 4 hours with periodic shaking to redisperse the powders. The ion-exchanged powders were centrifuged at 3500 rpm and washed several times with DI water to remove ions remaining in solution, then dried at 60 °C.

C. Exfoliation

To exfoliate individual nanosheets, the proton-exchanged powder was added to 50 ml of 2 wt% tetrabutylammonium hydroxide (TBA-OH) in a plastic centrifuge tube and put in an ultrasonic bath for 4 hours, with manual shaking every 30 minutes to redisperse the powder. The suspension was centrifuged at 3500 rpm for 20 minutes to separate the remnant birnessite powder from the nanosheet suspension. The suspension was decanted into a separate container and saved, while the powders at the bottom of the tube were redispersed in DI water by manual shaking and subsequent centrifuging. Each redispersion step produced a new suspension of nanosheets that was collected and saved.

Exfoliation of the same suspension composition was also performed using a vortex mixer and orbital mixer. In addition, exfoliation was attempted on the parent phase material using the ultrasonic bath procedure given above.

D. Flocculation

Flocculation of the nanosheets was achieved through the addition of acid or salt solutions. Aqueous solutions used in this work include HCl, LiCl, Li₂CO₃, NaCl, and Na₂CO₃. In the case of HCl, enough was added to bring the suspension to a pH of 1, 2, or 4. For other salts, 5 ml of 1 molar salt solution was added to 45 ml of suspension. The suspensions were allowed to stir for 12 hours to reach equilibrium prior to washing and collecting via centrifugation. The resulting floccules were washed to a neutral pH for acid-flocculated samples, or by replacing the water and centrifuging the suspension 3 times for salt-flocculated samples. The suspension pH was monitored using an accumet AB150 pH meter.

Flocculated materials were dried in air under two conditions: directly from the aqueous suspension after washing, which was performed at 60 °C in an oven, or by replacing the water with isopropanol and evaporating the alcohol at room temperature.

E. X-ray Diffraction

XRD patterns were collected on a Bruker D8 Advance diffractometer equipped with a Cu-K α source with a Ni metal filter and a LYNXEYE XE position-sensitive

detector. The sample was set to spin at 30 rpm. For nanosheet restacking with high d-spacings, data was collected from 3-70 °2 θ .

High-temperature XRD was performed on a Bruker D8 Advance diffractometer using Cu-K α radiation, an Anton Parr HTK 1200N furnace, and a VÅNTEC-1 detector. Flocculated nanosheets were dried onto a clean sapphire disc for measurement. Patterns were collected up to 800 °C from 5-70 °2 θ .

F. Scanning Electron Microscopy

Electron micrographs were collected using an FEI Quanta 200F Environmental Scanning Electron Microscope equipped with an EDAX energy-dispersive spectrometer. Dry samples were mounted by dusting powder onto carbon tape on an aluminum stub. Wet samples were dried onto carbon tape on an aluminum stub in a drying oven at 60 °C. Bulk powders were imaged using an accelerating voltage of 20 kV at a working distance of approximately 10 mm. Nanosheet samples were imaged at accelerating voltages of 2 and 5 kV at working distances between 6 and 10 mm.

G. Thermogravimetric Analysis

Thermogravimetric analysis was performed using a TA SDT Q600 TGA instrument. Samples were measured under flowing air (100 ml/min) from room temperature to 800 °C at a rate of 20 K/min in platinum pans. The sample mass used was approximately 20 mg. Simultaneous differential scanning calorimetry (DSC) was performed by comparing the sample against an empty platinum reference pan.

H. Surface Area Measurement

The surface areas of synthesized and processed materials were measured using a Micromeritics TriStar II Surface Area and Porosity Instrument. The surface area was calculated using the BET method at liquid nitrogen temperatures using N₂ gas. The powders were degassed in a Micromeritics FlowPrep 060 Sample Degas System at 150 °C for 4 hours under flowing N₂ prior to measurement.

I. Electrochemical Measurement

Capacitance values were measured using a CH Instruments Electrochemical Analyzer CHI6015E. Using a platinum counter electrode and a KCl reference electrode, chronopotentiometry and cyclic voltammetry experiments were conducted on MnO₂ nanosheets and floccules deposited on fluorine-doped tin oxide (FTO) coated glass. Methods of electrode preparation included drop casting, spray casting, and tape casting. Drop casting was performed by drying aqueous suspensions of nanosheets or floccules onto a cleaned FTO surface at 60 °C. Spray casting was performed by heating the FTO substrate on a hotplate at 100 °C and using pressurized air to spray suspensions of nanosheets or floccules through a capillary onto the surface. Tape casting was performed by intimately mixing dried MnO₂ nanosheet floccules with a binder formed from carbon black and polyvinylidene fluoride (PVDF) in a mass ratio of 80:5:15. N-methyl-2-pyrrolidone (NMP) was added to allow a magnetic stir bar to spin and mix the powders. The powders were mixed for 6 hours, tape cast on the FTO surface, and dried in a vacuum oven at 120 °C for 4 hours.

RESULTS AND DISCUSSION

A. Synthesis

Birnessite (δ -MnO₂) can be synthesized using several different processes, including aqueous precipitation, hydrothermal synthesis, and solid-state synthesis. The amount and type of cation in the interlayer is easily controlled when forming birnessite through hydrothermal and aqueous precipitation routes, but the quality of the crystal suffers due to the low temperature of synthesis. High-quality crystals of δ -phase MnO₂ can be formed using solid-state synthesis, but, of the cations studied, only potassium formed a phase-pure material after treatment at 900 °C. Through solid-state synthesis, birnessite forms directly at temperatures below 900 °C when K₂CO₃ and MnCO₃ are mixed and heated in air.

The phase purity and microstructure of birnessite synthesized via solid-state techniques was analyzed using scanning electron microscopy and x-ray diffraction. Due to the high-temperature conditions of synthesis, the diffraction peaks are very sharp, especially compared to commonly-studied natural forms of birnessite and those produced by other methods such as hydrothermal synthesis. The solid-state method of producing synthetic birnessite is preferred due to the quality of the crystal. The difference in peak full-width at half maximum (FWHM) between birnessite synthesized via different routes cannot be discounted. The XRD patterns shown in Figure 8 give a good indication of the difference in crystallite size and/or perfection of the synthesized birnessites. The hexagonal packing of MnO₆ octahedra is visible in the grains of the parent phase, as shown in Figure 6 where the facets and stacking faults are clearly visible.

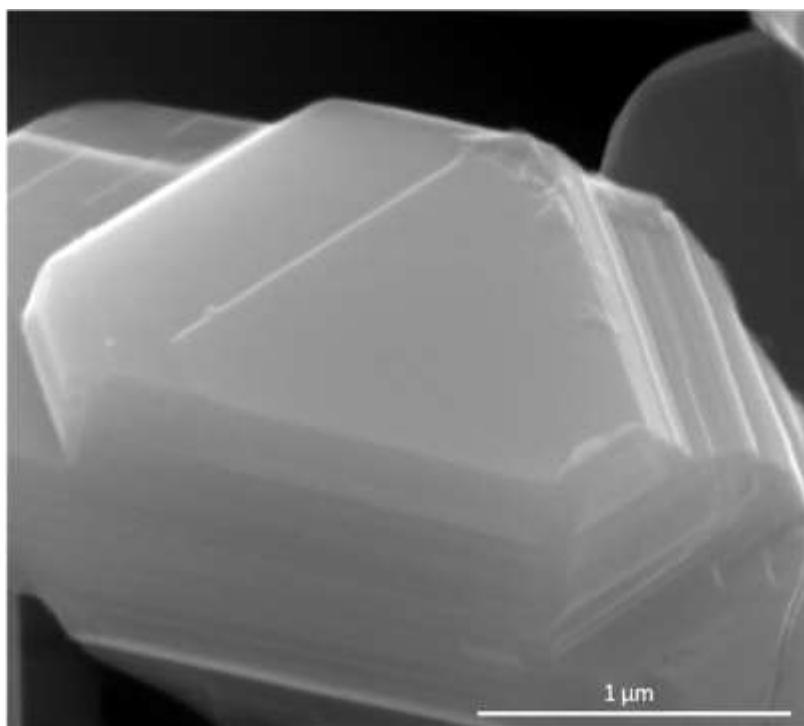


Figure 6. Parent-phase $K_{0.45}MnO_2$ prepared by solid-state synthesis showing faceting and hexagonal symmetry.

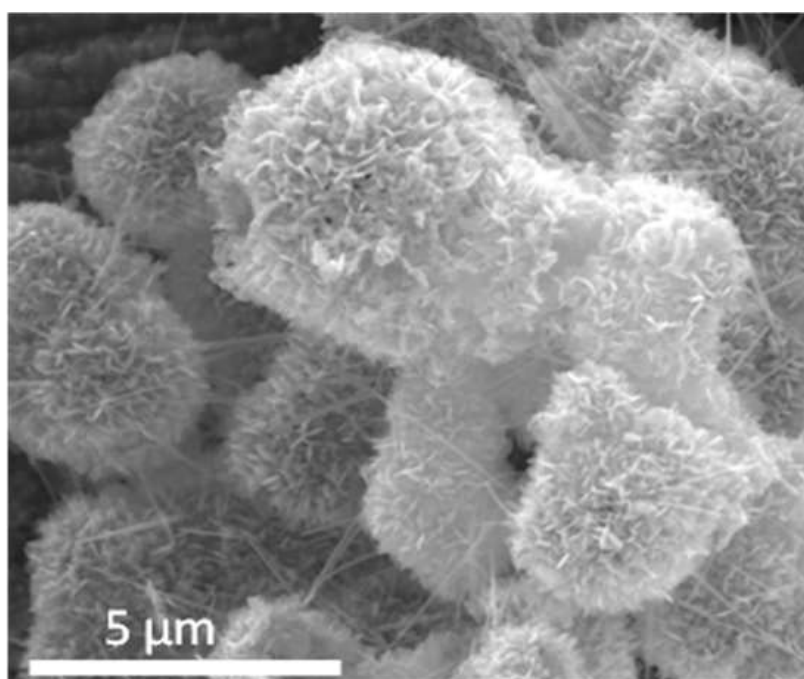


Figure 7. Hydrothermally-grown δ - MnO_2 nanoflowers and α - MnO_2 nanowires.

One of the goals of this study was to investigate the roles of defects on the electrochemical performance of MnO₂-based electrochemical supercapacitors. Starting from highly-crystalline and nominally defect-free crystals, the quantity and nature of defects in the final nanosheet structures can be more easily controlled and compared to sheets formed hydrothermally.

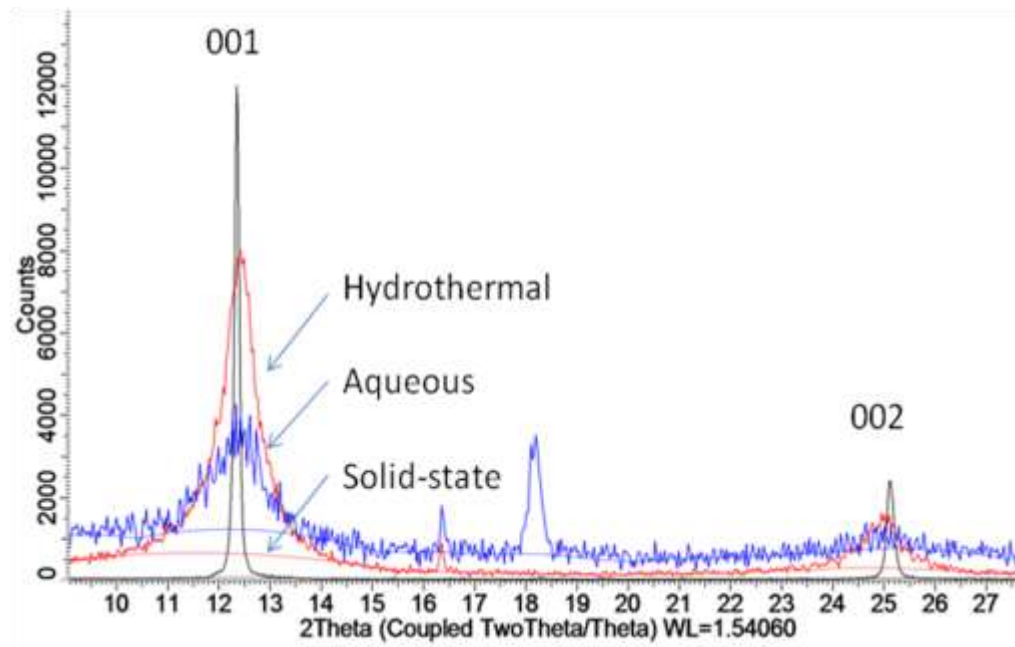


Figure 8. XRD of birnessite synthesized by solid-state (black), hydrothermal (red) and aqueous precipitation (blue) methods.

The nanoflowers shown in Figure 7 were synthesized via hydrothermal synthesis, with aqueous KMnO₄ used as the reagent. Via the same process, it was possible to synthesize both aqueously suspended nanoflowers and to grow nanoflowers on nickel foil substrates with the same morphology. XRD performed on zero-background holders suggests that the nanoflowers are stacking-disordered δ -MnO₂ due to the broadening of the (001) and (002) peaks. The broadening of higher angle ($hk0$) peaks indicates additionally poor in-plane crystallinity. Using the same process, it was not possible to deposit nanoflowers on nickel foam. The difference between the nickel foam and the nickel foil was not investigated to determine the cause for this disparity.

By mixing Mn²⁺ salts such as manganese acetate with hydroxides in water, it was possible to precipitate birnessites with different interlayer cations of the form A_xMnO₂.

The hydroxide cation nature determined the layering cation, A, thus through the use of LiOH, NaOH, KOH, etc, it was possible to synthesize various birnessites where the MnO₂ sheets are separated by the hydroxide countercation. As above noted for the K-birnessite prepared by hydrothermal synthesis, the resulting δ -MnO₂ was of low quality and was not phase-pure, and was therefore not pursued.

The Mn source for birnessite formation using solid-state techniques must be specified in order to synthesize the correct phase. Groups have reported forming δ -MnO₂ from MnO₂ and K₂CO₃,¹⁹ and KMnO₄.²² Starting with Mn₂O₃, however, did not work with the synthesis parameters used in this study, but the desired final product was obtained through the calcinations of MnCO₃ and K₂CO₃, which has been previously reported from our group at Alfred University.⁵⁶

For this work, the initial target potassium content was a ratio of K:Mn of 0.45:1, based upon work by Omomo, et al. that reported on birnessite with the composition K_{0.45}MnO₂.¹⁹ This composition was made by mixing stoichiometric amounts of K₂CO₃ and MnCO₃. This K:Mn ratio, however, is not a requirement to achieve a phase-pure material. In order to better understand the interlayer spacings, water retention in the birnessites and other factors that might influence the 001 peak locations measured using XRD, the stoichiometry of K_xMnO₂ has been studied over the K range of x=0.35-0.60 (Figure 10). Through the heat treatment of KMnO₄, an additional x=1 birnessite sample was synthesized.

Increasing the K:Mn ratio in the compound K_xMnO₂ results in slight shifts of the basal (001) diffraction peaks over the range x=0.35 to x=1. As x increases, the diffraction peaks shift to higher angle, indicating a change in interlayer spacing. This is likely due to a difference in hydration of the interlayer, which stabilizes the expansion. In the high-temperature XRD, a reversible shrinkage of the interlayer is observed between 150 and 200 °C, indicating dehydration upon heating, as shown in Figure 9.

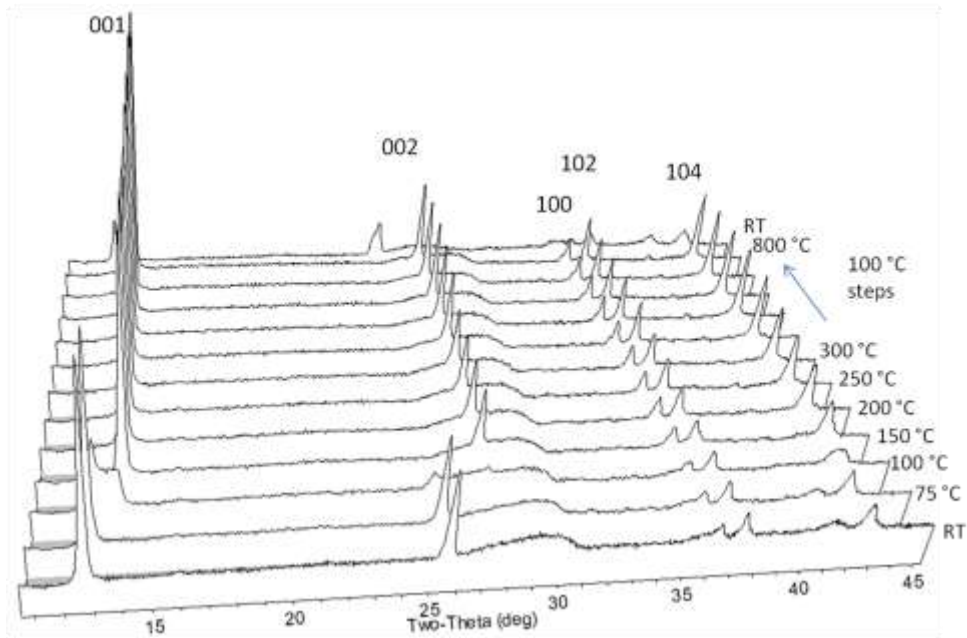


Figure 9. HTXRD of parent phase birnessite in air.

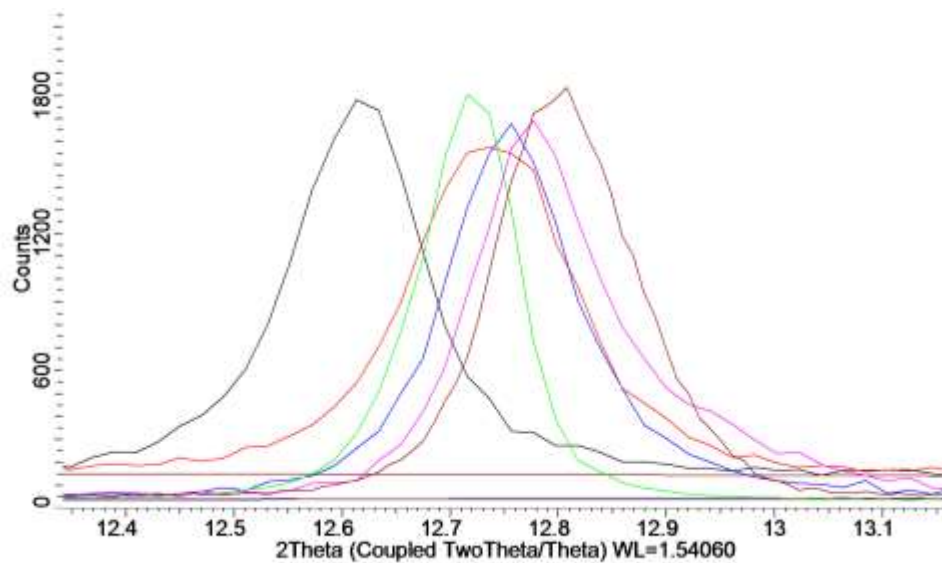


Figure 10. XRD of the K_xMnO_2 001 peak for $x=0.35$ (black), 0.40 (red), 0.45 (blue), 0.50 (green), 0.55 (pink), and 0.60 (brown).

The influence of water in the interlayer was tracked using high temperature diffraction. Above 150-200 °C, a reversible peak shift of approximately 1 °2θ occurs, representing a shift from an interlayer spacing of 6.95 to 6.41 Å ($\Delta d=0.54$ Å). Water loss

is also observed in TGA measurements. Figure 11 shows the TGA curve for the $x=0.45$ sample, which indicates a mass loss of approximately 6.5% up to 150 °C, which is approximately equivalent to 0.4 H₂O per birnessite formula unit. This value is lower by approximately 50% than reported values for hydrothermally synthesized birnessites,^{39,57} but the temperature of dehydration matches results by Johnson and Post.³³

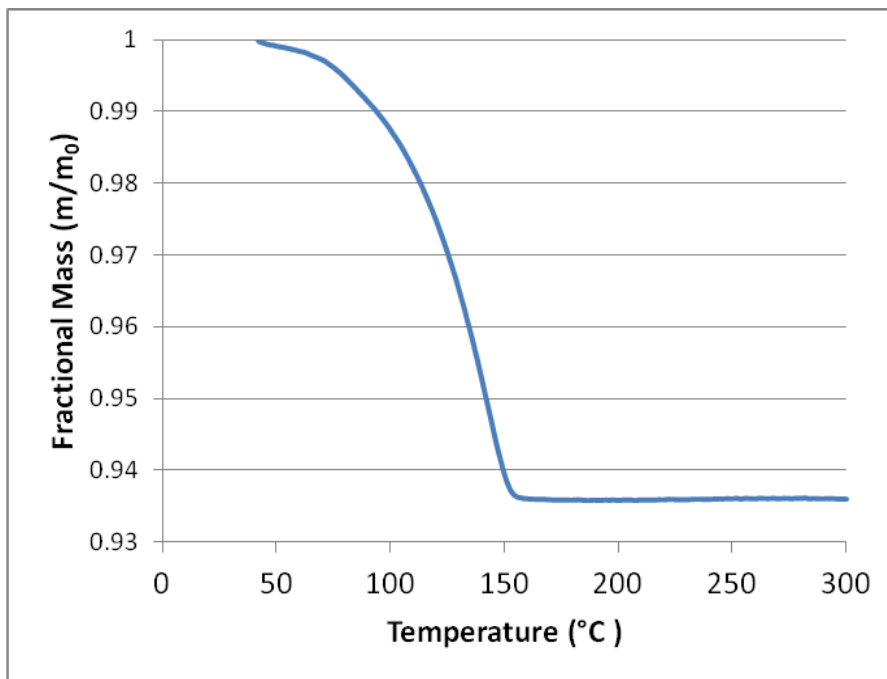


Figure 11. Mass loss on heating parent phase birnessite in air at 20 K/min.

Using solid-state synthesis, the only stable birnessite phase synthesized included only potassium in the interlayer. The addition of even a small amount of Na⁺ or Ca²⁺ in place of K⁺ results in a phase-impure sample. K_{0.4}Na_{0.05}MnO₂ forms a phase mixture of α - and δ -MnO₂, for example (Figure 12, Figure 13). As seen in Figure 12, even replacing one in nine potassium with sodium causes the growth of an α -MnO₂ phase during solid state synthesis. The same result was found when replacing K with Ca. This indicates that only the potassium form of birnessite is stable at high temperatures. Therefore, in order to change the layering cation, either different synthesis routes must be used or the potassium must be exchanged for different ions post-synthesis. The next section provides results for the ion-exchange process.

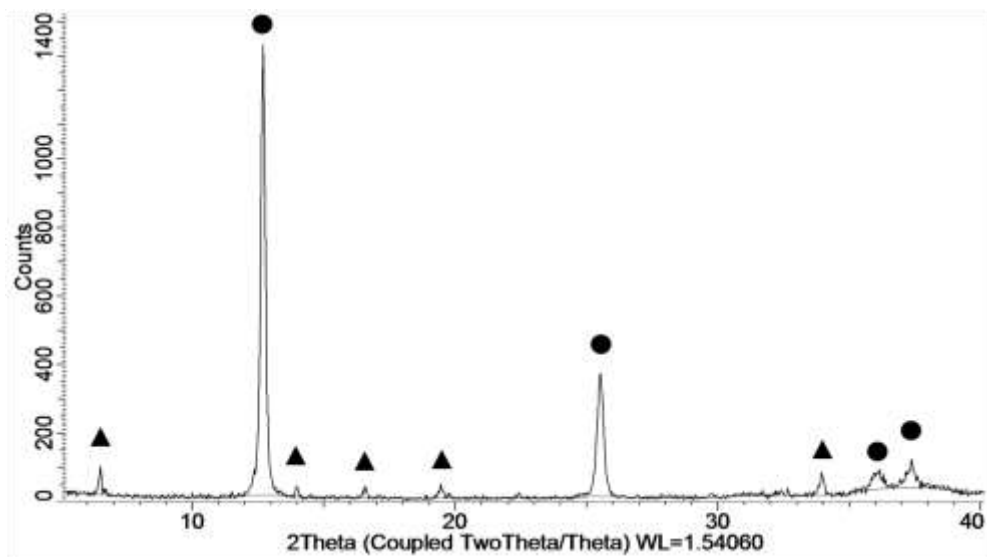


Figure 12. XRD of $K_{0.40}Na_{0.05}MnO_2$ showing growth of α - MnO_2 (\blacktriangle) and δ - MnO_2 (\bullet).

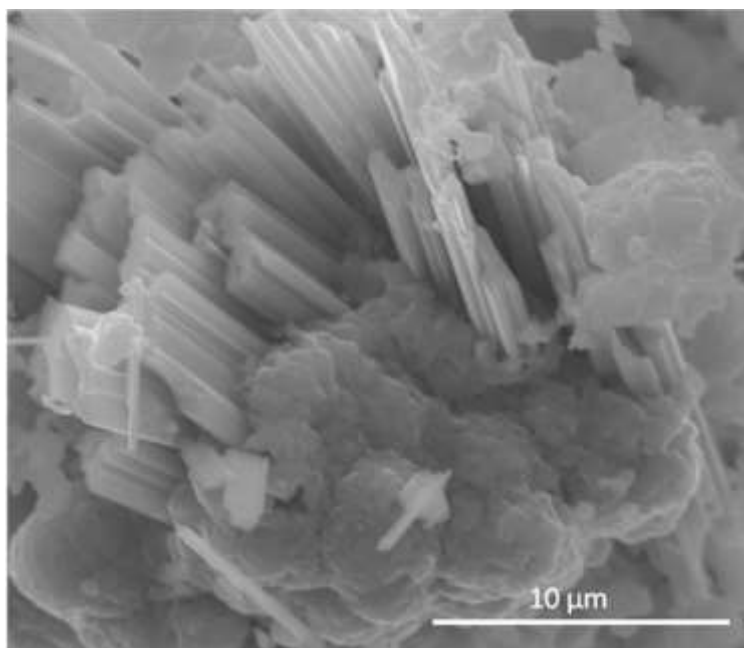


Figure 13. $K_{0.40}Na_{0.05}MnO_2$ microstructure with regions of tube-like α - MnO_2 and plate-like δ - MnO_2 .

It is also possible to substitute cations on the manganese sites, rather than in the interlayer. Work was done to replicate literature reporting the substitution of copper and iron on the manganese sites, as reported by Takei, et al.⁵⁸ These powders were found to be phase-pure by powder x-ray diffraction (Figure 14). Proton ion-exchanged powders

were taken to Oak Ridge National Laboratory (ORNL) to be characterized using neutron diffraction, but the high water content of the powders rendered the data insufficient for structural refinement work. Copper and iron were chosen for this purpose due to their neutron scattering cross sections, which differ greatly from that of manganese.

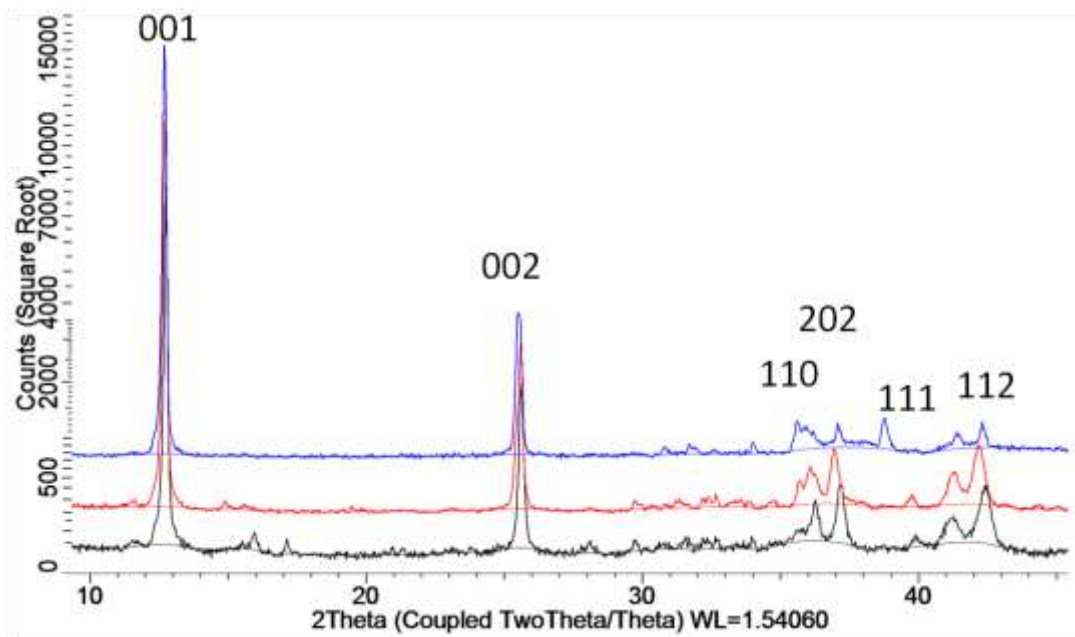


Figure 14. Parent-phase birnessite (black, bottom) substituted with copper (blue, top) and iron (red, middle) on a square-root scale.

B. Ion Exchange

Ion exchange of the interlayer potassium is possible due to the mobility of ions in the interlayer between the oxide layers. This has the effect of expanding the interlayer gallery enough that it can be observed in the XRD patterns, as in Figure 15. The extent of ion exchange was tracked using EDS (Table I). It was found that after two ion exchange steps in acid over 90% of the interlayer potassium was removed and replaced with protons.

Table I. XRF Potassium Content Analysis

	K:Mn Ratio
Parent phase	0.45
First ion-exchange	0.094
Second ion-exchange	0.038

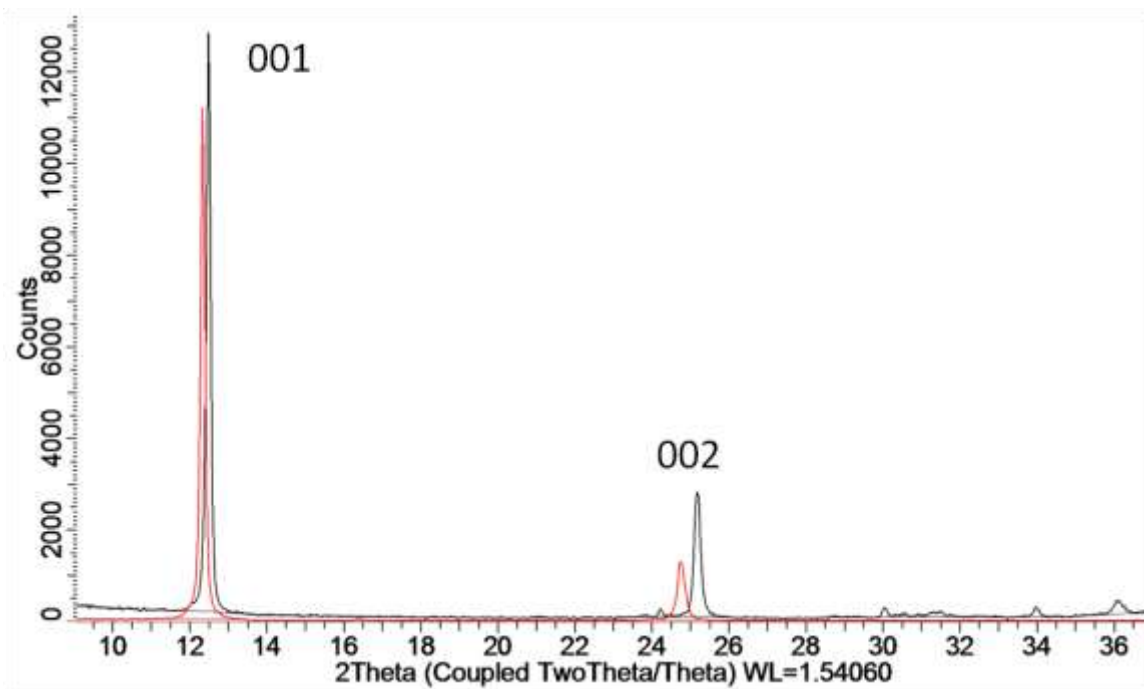


Figure 15. Shift in basal peaks from the parent-phase (black) to the proton-exchanged phase (red).

Ion-exchanges were also performed using LiCl, NaCl, KCl, MgCl₂, SrCl₂, and ZnCl₂ using both the proton-exchanged and parent-phase birnessites as precursors. These ions were chosen to mimic literature reporting on the exchange or synthesis of birnessites with the same layering cation.^{28,29,34,35,37,59} The samples exchanged with the proton-exchanged MnO₂ had more of the cation successfully exchanged, and these samples were the ones used for further testing. The extent of exchange as quantified by EDS is given in Table II. Lithium content cannot be easily measured via EDS and is therefore omitted. The initial loading for each exchanged cation was 0, as all layering cations were replaced with protons prior to further treatment.

Table II. Cation Ion Exchange Analysis

Cation	Cation:Mn Ratio
Na	0.03:1
K	0.05:1
Mg	0.02:1
Sr	0.02:1
Zn	0.24:1

C. Exfoliation

The ion exchange step is a necessary one for exfoliation. Directly trying to exfoliate the parent phase sample through the addition of TBA-OH does not result in any significant production of nanosheets. This is likely due to the strong interlayer bonding resulting from the potassium ions. The interlayer attraction must first be weakened by exchanging the potassium with H^+ , H_2O , and H_3O^+ , during which process the interlayer gallery expands. Exfoliation is achieved through the insertion of bulky organic TBA^+ ions into the interlayer, which has the effect of separating the layers enough so that they can be dissociated through physical means, such as shaking. Nanosheets exfoliated in this fashion are sufficiently thin and well-dispersed enough that they form a stable suspension. It is possible to separate the exfoliated nanosheets from the remnant bulk powder through centrifugation. When these powders are redispersed in deionized water, more nanosheets free themselves and form a suspension. From the observed clarity of the suspensions, each redispersion produces suspensions with lower mass loadings than the ones before until the point where additional redispersions do not form suspensions with any observable nanosheet content. This typically is on the order of 10 redispersions.

The residual powders left after centrifugation are a mix of an un-exfoliated proton-exchanged phase and a TBA-pillared phase, where the interlayer has been expanded further from the ion-exchanged phase but still presents an ordered crystal with sharp diffraction peaks, as seen in Figure 16. The (001) spacing, representing the size of the sheet and the interlayer gallery, expands upon intercalation of TBA^+ , increasing from 7.15 Å to 12.40 Å, as evidenced by the appearance of a new basal series appearing, starting at $7^\circ 2\theta$. A TBA ion is tetrahedral, and approximately 8.4 Å in length,¹⁹ but the increase in interlayer spacing is only 5.25 Å, indicating that the TBA^+ replaces or otherwise fits in along with prior interlayer molecules, such as water.

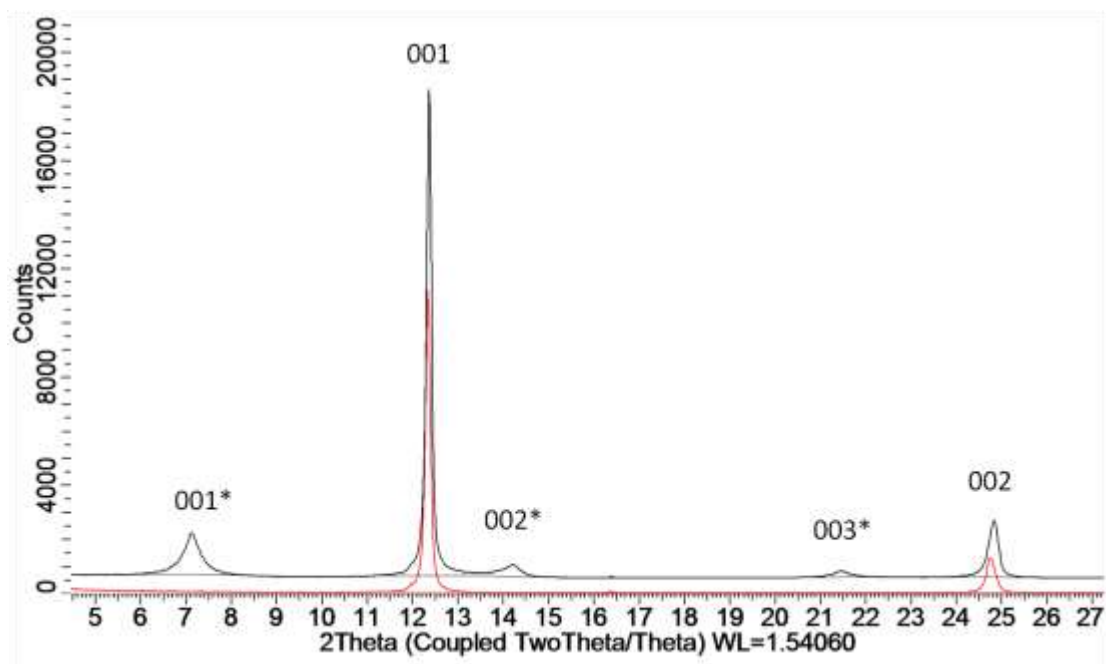


Figure 16. Unexfoliated powder remaining after centrifugation of nanosheets (black) with the proton-exchanged pattern (red) overlaid showing a pillared phase (*).

The lateral dimensions of the exfoliated sheet can be adjusted via the exfoliation route. Several different such routes are available, including orbital mixing, stirring, vortex mixing, and treating with an ultrasonic bath. The orbital mixer seemed to produce nanosheets microns in lateral size, while the ultrasonic bath only made sheets ~200-500 nm on a side. The size of the sheet was estimated from the size of the features observed in the SEM images, and an example is shown in Figure 17. Atomic force microscopy (Figure 18) supports lateral dimensions of hundreds of nanometers in the case of nanosheets exfoliated using an ultrasonic bath.

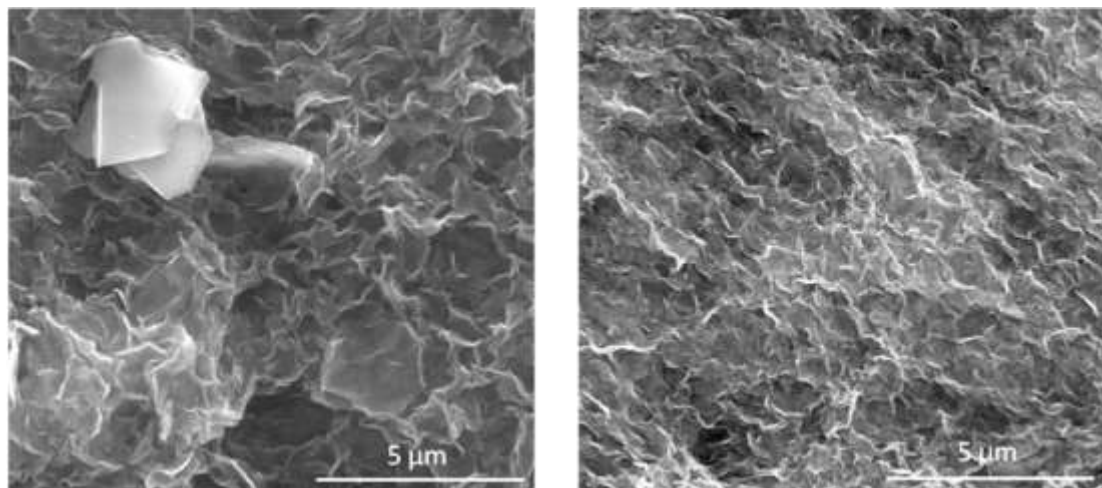


Figure 17. Flocculated nanosheets exfoliated via (left) orbital mixer and (right) ultrasonic bath dried from isopropanol.

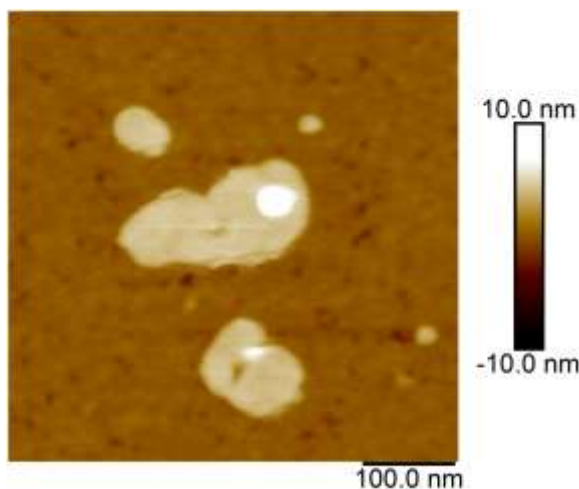


Figure 18. AFM of MnO_2 nanosheets with a thickness of 3.8 nm.

It is possible to confirm the presence of nanosheets in the suspension using XRD. By drying several drops of the suspension on a zero-background sample holder in an oven at 60 °C, the nanosheets restack into loose layers separated by water and TBA, resulting in strong $(00l)$ reflections, as shown in Figure 19. The in-plane diffraction peaks are generally not observed because of the nanosheet orientation on the sample holder.

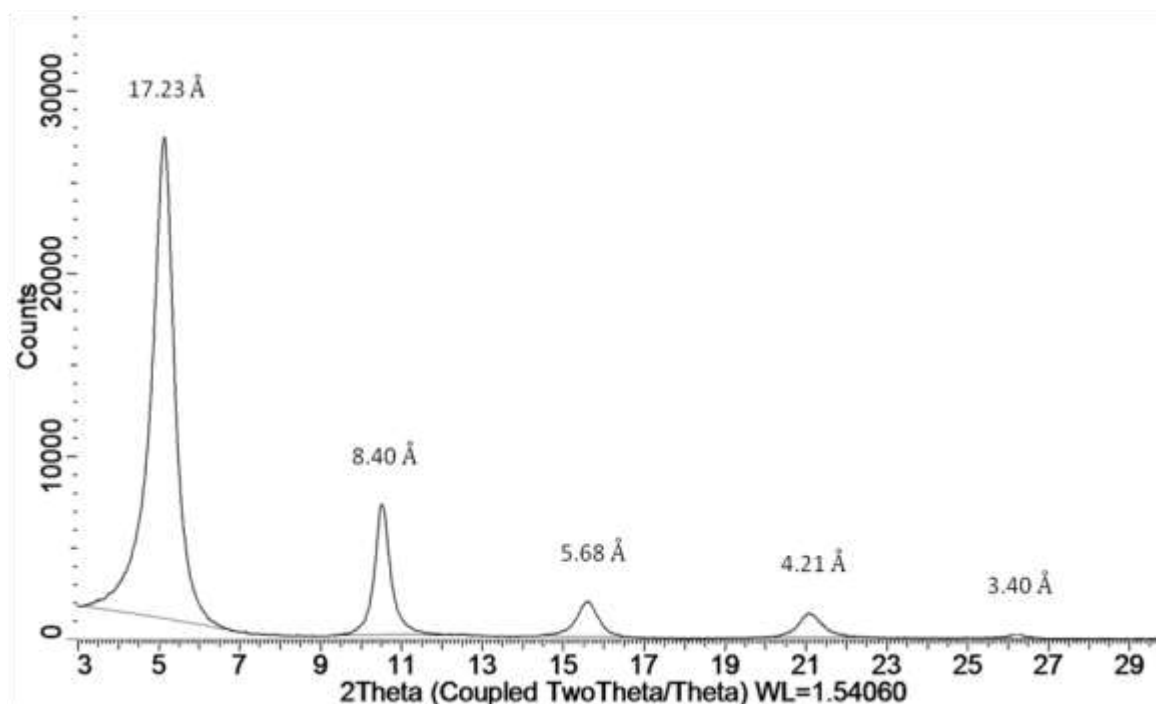


Figure 19. Dried nanosheet suspension showing restacked 00l peaks.

D. Flocculation

The addition of HCl, LiCl, or NaCl destabilizes the nanosheet suspension and causes the nanosheets to agglomerate via flocculation. The nanosheets form macroscopic groupings that are large enough to settle out of suspension and be collected. The XRD patterns of the dried nanosheets suggests small amounts of restacking between sheets in the flocculated samples, as evidenced by the broad basal peaks present in the diffraction patterns. The morphology of the flocculated and dried samples was imaged by SEM and seems to comprise rumbled and bent sheets forming an open 3D network. BET measurements (Figure 20) indicate that the floccules have surface areas on the order of 100 m²/g.

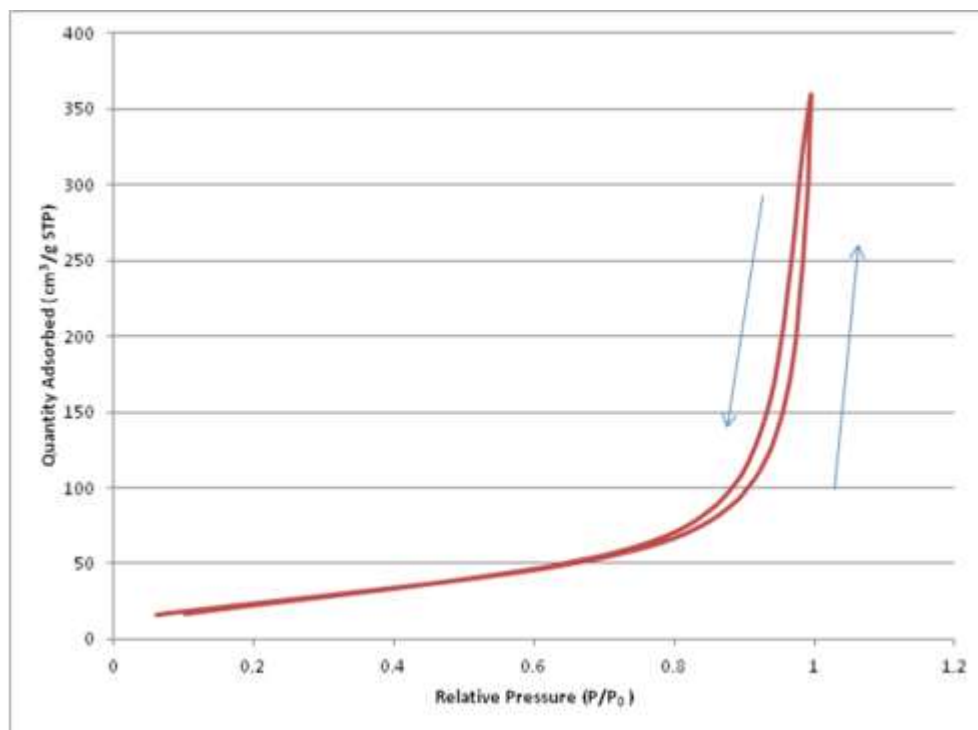


Figure 20. BET of MnO₂ nanosheets flocculated at pH 2 using HCl. SSA=94 m²/g.

The hysteresis loop presented in the BET data shown in Figure 20 has been characterized as deriving from slit-like pores.⁶⁰ The presence of slit-like pores indicates that the nanosheets have restacked to form loose layered structures with stacking distances large enough to create mesoporosity. For applications related to catalysis and capacitance, these restacked sheets may limit the available surface area and hence kinetics of reactions. If molecules or ions cannot diffuse between the sheets quickly enough, the response of films will be limited, resulting in slower charge and discharge rates or reduced overall capacity.

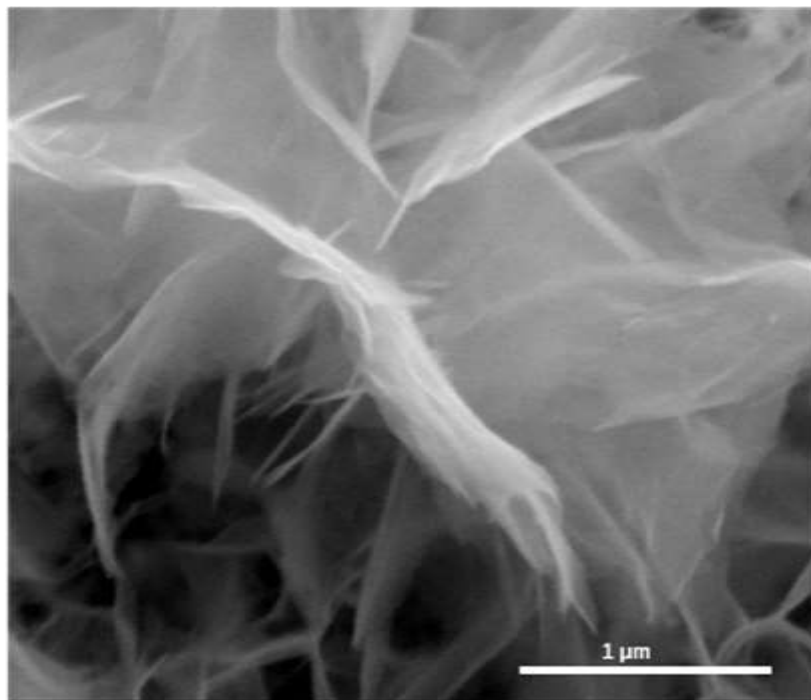


Figure 21. Nanosheets flocculated with HCl at pH 2, dried from an aqueous suspension at 60 °C.

The morphology of these floccules appears to be an open network formed from stacks of sheets randomly connected together. The size of the sheet affects the packing, with larger sheets having more steric hindrances that result in a more porous and open network. Small sheets form smaller pores, resulting in denser microstructures (Figure 17). The method of drying also affects the final microstructure. Floccules dried from aqueous suspensions exhibit the most visible restacking and densest microstructures observed in the SEM. Figure 21 shows floccules with large sheets that form an open network due to steric effects, but also show significant restacking in the center of the micrograph. It is also possible to exchange the water in the suspension for an alcohol such as isopropanol prior to drying. This results in less restacking and more open pore networks in the SEM micrographs.

It is possible to add nanosheet suspensions to suspensions of other particles and sheets and flocculate the nanosheets to form nanocomposites. Upon the addition of flocculating agents such as those noted previously, the MnO₂ nanosheets will flocculate and capture other suspended media. This has been shown with suspensions of

nanocrystalline TiO₂ (P25, Degussa) and carbon black. When P25 was added to a suspension of nanosheets (0.5 grams in 50 ml), it dispersed without settling out of suspension. Upon the addition of HCl to flocculate the nanosheets, the entire suspension flocculated together, P25 and MnO₂ alike. A similar suspension of only dispersed P25 did not flocculate with the addition of HCl. Fine dispersions of powder can therefore be sequestered by flocculating nanosheets in the same suspension. These materials were not pursued further as part of this work.

E. Defects in MnO₂ Nanosheets

A reduction of Mn from 4+ to 3+ upon equilibrating in HCl causes in-plane stress due to the Jahn-Teller distortion of the MnO₆ octahedra. Models from Manceau, et al, suggest that defects in the MnO₂ sheet take the form of Mn³⁺ octahedra that move from the in-plane configuration to a surface-coordinated position as a sort of “surface Frenkel defect.” In order to characterize the defects formed through processing of the MnO₂ nanosheets, x-ray total scattering experiments were performed at the Argonne National Laboratory Advanced Photon Source synchrotron by Peter Metz of Alfred University using samples prepared by the author. Using data collected there, pair-distribution function (PDF) modeling was performed to track the ratio of in-plane to out-of-plane manganese octahedra. As seen in Figure 22, the ratio of in-plane to out-of-plane manganese decreases as a function of treatment pH. All data was normalized to the Mn-O distance of 1.896 Å. The in-plane peak at 2.86 Å shows the highest intensity in the parent-phase sheets and lowest in sheets flocculated at pH 2. Conversely, the out-of-plane peaks at 3.4 Å shows an increase of surface-coordinated octahedra after pH treatment.⁶¹ This indicates that it is possible to control the defect content by controlling processing parameters, most notably the flocculation equilibrium pH.⁵⁶

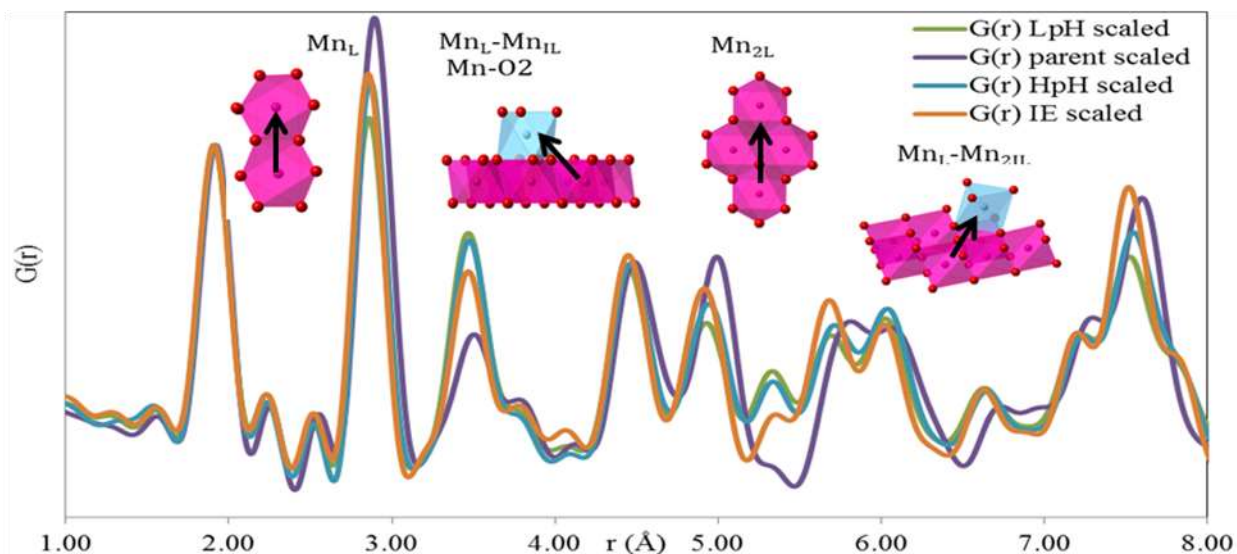


Figure 22. PDF analysis of MnO_2 defects as a function of processing.⁶¹

F. Electrochemical Performance and the Role of Defects

Due to its large number of valence states and the ease with which the state can be changed, manganese is a good candidate for electrochemical charge storage. The sheet primarily contains Mn^{4+} .⁵⁶ In an electrochemical cell with sodium sulfate as an electrolyte, the valence state can be changed to 3+ with Na^+ as a charge balancing ion associated with the sheet surface. Electrochemical films formed by either drip casting or tape casting onto conductive fluorine-doped tin oxide (FTO)-coated glass or Ni foil were tested via cyclic voltammetry or chronopotentiometry to determine the viability of the approach. Work done with Peng Gao of Alfred University was used to determine the specific capacitance of electrodes formed via these methods.⁵⁶ Sheets flocculated at pH 4 had a specific capacitance of 209 F/g, while sheets flocculated at pH 2 had a specific capacitance of 306 F/g.

G. High-Temperature Phase Stability and Phase Transitions to Form Tunnel-structured α - MnO_2

High-temperature XRD and TGA were performed, along with supplemental SEM, to characterize the effects of heating on these nanostructured materials.

1. Parent phase

As discussed previously, the as-synthesized phase is stable to at least 800 °C as observed by HTXRD, with a reversible dehydration of the interlayer occurring between 150 and 200 °C (Figure 23).

After the parent-phase birnessite has undergone any amount of wet chemical processing, it loses its high-temperature stability. Even washing the parent-phase material in water causes a secondary phase to grow upon subsequent heating to 800 °C. While the original diffraction pattern is similar to the unaltered parent phase, above 600 °C a second phase forms and persists even after the sample is cooled to room temperature. This second phase can be identified as α -MnO₂. The phase destabilization is likely due to the aqueous dissolution of some of the interlayer K⁺ ions. Adding 0.5 grams to 50 ml of water rapidly increases the pH to greater than 12. Since adding birnessite to water causes the pH to increase, this seems likely to be due to the scavenging of H⁺ by the interlayer of the birnessite, which changes the order of the interlayer by displacing K⁺ ions and associating with the sheet surfaces.

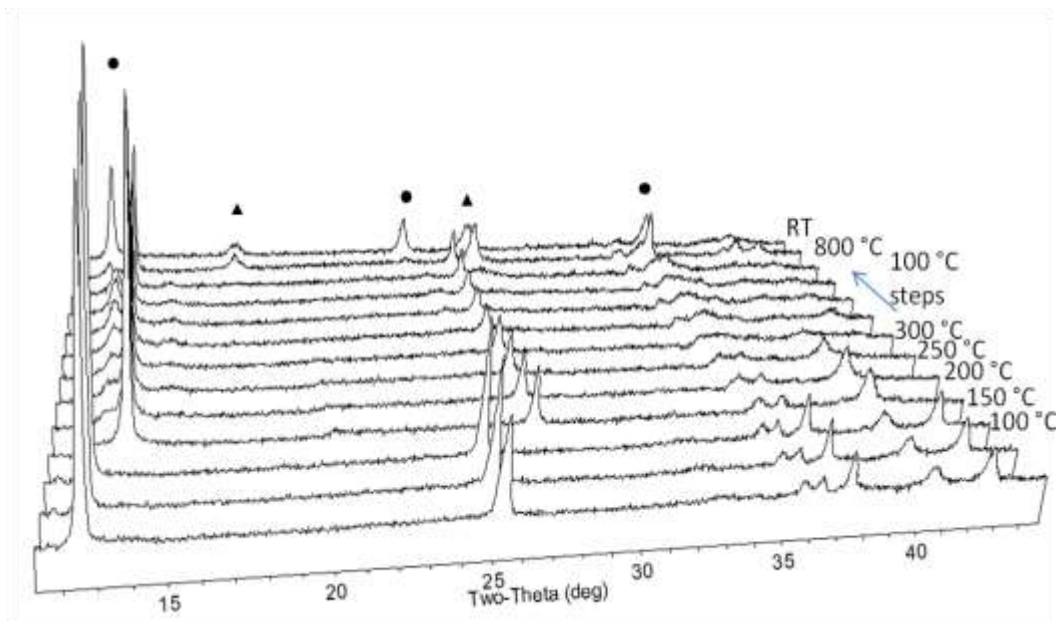


Figure 23. HTXRD of parent-phase birnessite (●) washed in water showing growth of α -MnO₂ (▲).

2. Ion-exchanged phase

HTXRD was performed on ion-exchanged powders. In each case, above 200 °C the basal reflections disappear completely, leaving an x-ray amorphous sample between 200 and 600 °C. Starting at 600 °C, new phases begin to appear in the diffraction pattern. These phases all remain after the sample is cooled back to room temperature. The phases that appear depend on the identity of the cation exchanged, and are given in Table III. In each case, a small amount of the tunnel phase α -MnO₂ formed along with Mn₂O₃ and Mn₃O₄. In the case of the Na-exchanged phase, the tunnel phase is observed to form prior to the growth of Mn₂O₃, as shown in Figure 24.

Table III. Cations Exchanged and Phase Composition After 800 °C Treatment

Exchanged Cation	Mn ₂ O ₃ present	α -phase present	Other phases
H ⁺	Yes	Yes	N/A
Li ⁺	Yes	Yes	Li ₄ Mn ₅ O ₁₂ (spinel)
K ⁺	Yes	Yes	Mn ₃ O ₄
Na ⁺	Yes	Yes	N/A
Mg ²⁺	No	Yes	MgMn ₂ O ₄
Sr ²⁺	No	Yes	Mn ₃ O ₄
Zn ²⁺	No	Yes	Zn _{0.75} Mn _{2.25} O ₄

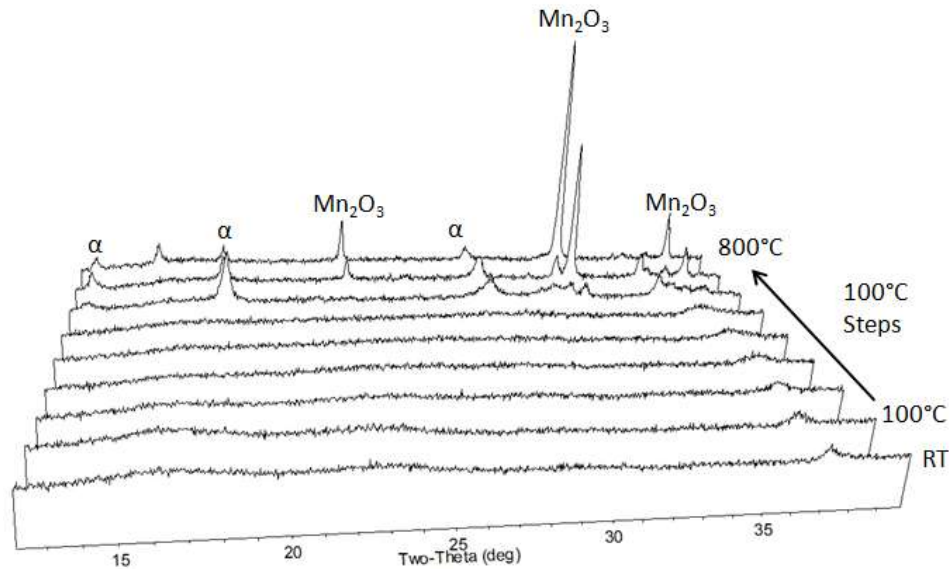


Figure 24. Growth of α -MnO₂ from Na_{0.03}MnO₂ as seen in HTXRD.

The presence of cations larger than Li^+ (Na^+ , Ca^+ , etc.) appears to stabilize a small amount of $\alpha\text{-MnO}_2$, which has a 1-dimensional tunnel structure. This appears in the HTXRD as the growth of a cryptomelane phase. Li_xMnO_2 forms Li-spinel with MnO_2 of the form LiMn_2O_4 after heating in place of a tunnel-structured phase. In addition to these alkali-bearing phases, Mn_2O_3 and Mn_3O_4 formation is observed where the major phase appears to be controlled by the nature or size of the cation present. Polyvalent elements such as Mg, Sr, and Zn favor the growth of Mn_3O_4 and appear to substitute themselves into that lattice, as shown in Table III.

3. Flocculated material

Flocculated nanosheets appear as crumpled stacks in the SEM. Heating these in air to $800\text{ }^\circ\text{C}$ causes the sheet-like nature to disappear as the atoms gain enough mobility to lower their surface energy. The end result is a ceramic with a microstructure similar to that of spinodally-decomposed glass, with an open pore structure with pore sizes on the order of 200 nm . This process starts with small holes appearing in the sheets around $400\text{ }^\circ\text{C}$. At $500\text{ }^\circ\text{C}$, the sheet structure is visible at low magnification, but the microstructure resembles a spinodally-formed Mn_2O_3 . These microstructures are represented in the SEM images shown in Figure 25.

The flocculated samples in particular show large instabilities at high temperature. When flocculated with HCl and thus not introducing any alkali or alkaline earth ions, heating above $400\text{ }^\circ\text{C}$ causes the entire sample to transform into Mn_2O_3 . When other species are used as flocculating agents, such as NaCl, the growth of other phases is encouraged. In particular, Na^+ flocculation encourages the growth of the tunnel-structured $\alpha\text{-MnO}_2$. The low Na-loading of the floccules causes a phase mixture of Na- MnO_2 tunnels and Mn_2O_3 that is visible in the final morphology seen in the SEM. SEM images taken at increasing temperatures have shown the slow deconstruction of the sheet-like nature of $\delta\text{-MnO}_2$ as it transforms into Mn_2O_3 . As seen in the SEM images, originally the sample is composed of sheets hundreds of nm in lateral dimension (Figure 25a). As the temperature increases, pits and pockmarks begin to form, creating discrete holes in the sheets (Figure 25b). By $500\text{ }^\circ\text{C}$, the sheets have almost entirely been changed into a microstructure not unlike spinodally-decomposed glass, but at low magnifications the sheet macrostructure is still somewhat visible (Figure 25c). By $600\text{ }^\circ\text{C}$, however, even the

large-scale hints of a sheet network have disappeared and the sample appears to be a homogenous network of Mn_2O_3 with interconnected particles on the order of 100 nm thick and 100s of nm long (Figure 25d).

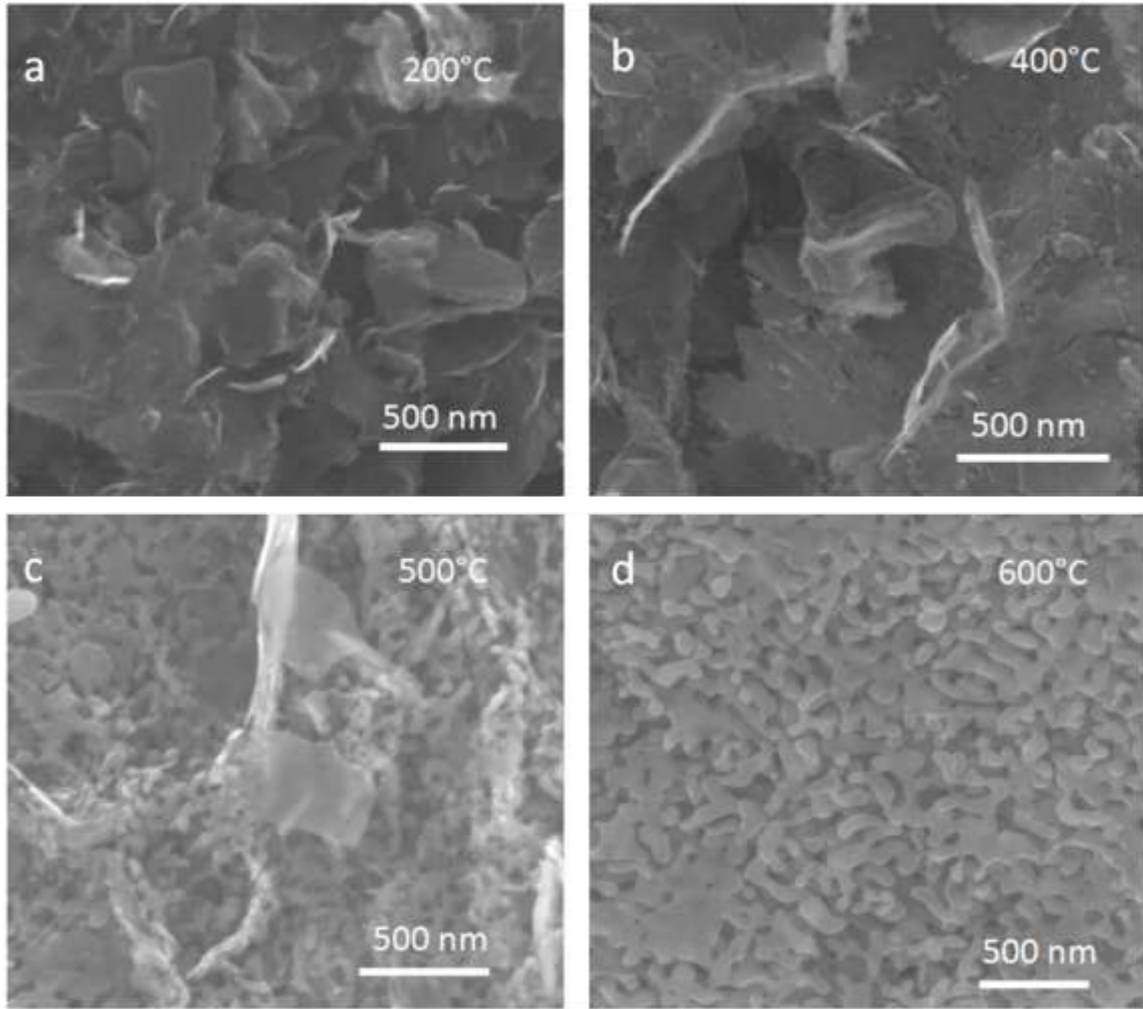


Figure 25. Microstructural evolution of MnO_2 floccules heated in air.

Prior work has been done on heat-treated samples of H-flocculated MnO_2 nanosheets that suggests that a tunnel structure can form as low as 200 °C, although this is not visible in lab-scale XRD data and was extracted from pair distribution function data collected at Argonne National Lab.⁶¹

Through modeling performed on flocculated MnO₂ created as part of this work, Peter Metz of Alfred University was able to fit the cryptomelane (α -MnO₂) structure to the measured PDF data (Figure 26).

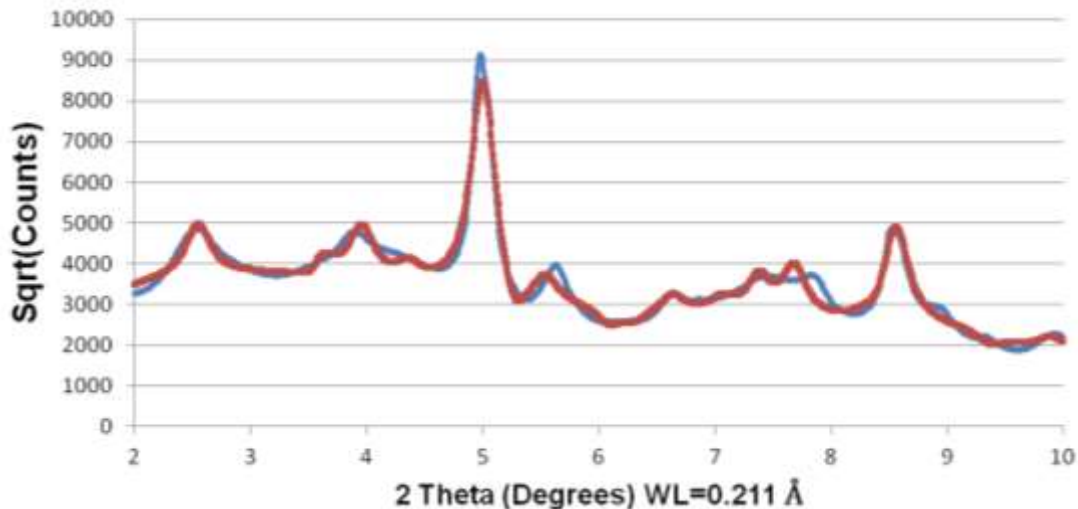


Figure 26. PDF data of H-flocculated MnO₂ (blue) with a cryptomelane structure fit (red), by Peter Metz.

HTXRD on nanosheets flocculated with LiCl and NaCl formed phases incorporating the alkali ion. Sodium in particular encouraged the growth of α -MnO₂ in addition to Mn₂O₃, and this is visible in both the XRD and SEM in Figure 27 and Figure 28, respectively. The Na-flocculated MnO₂ showed growth of the α phase at 600 °C prior to significant formation of Mn₂O₃, but Mn₂O₃ crystallized in greater quantity up to 800 °C.

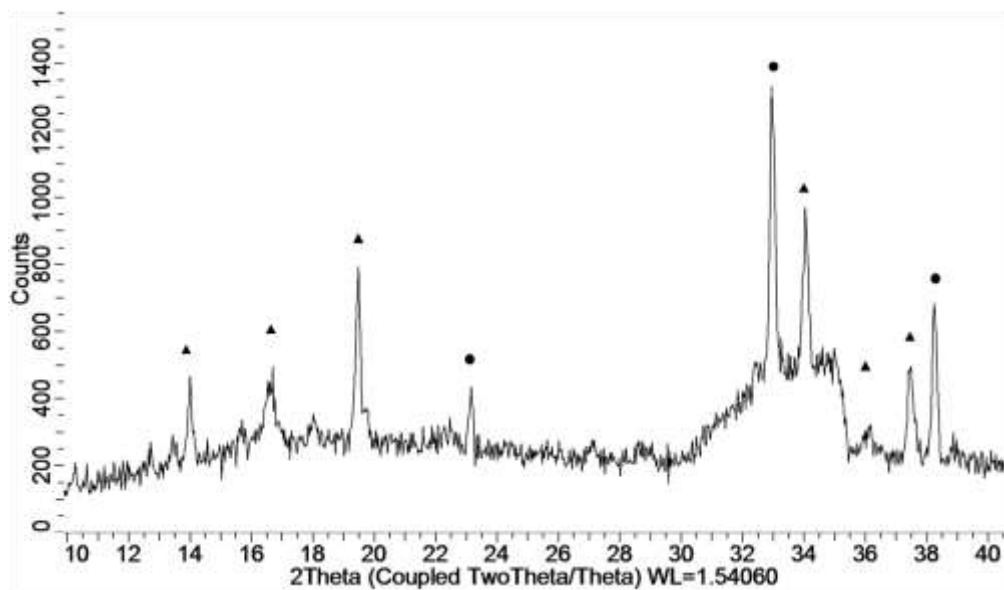


Figure 27. MnO_2 nanosheets flocculated with NaCl , heated to $800\text{ }^\circ\text{C}$ in air showing Mn_2O_3 (●) and tunnel-structured $\text{Na}_4\text{Mn}_9\text{O}_{18}$ (▲).

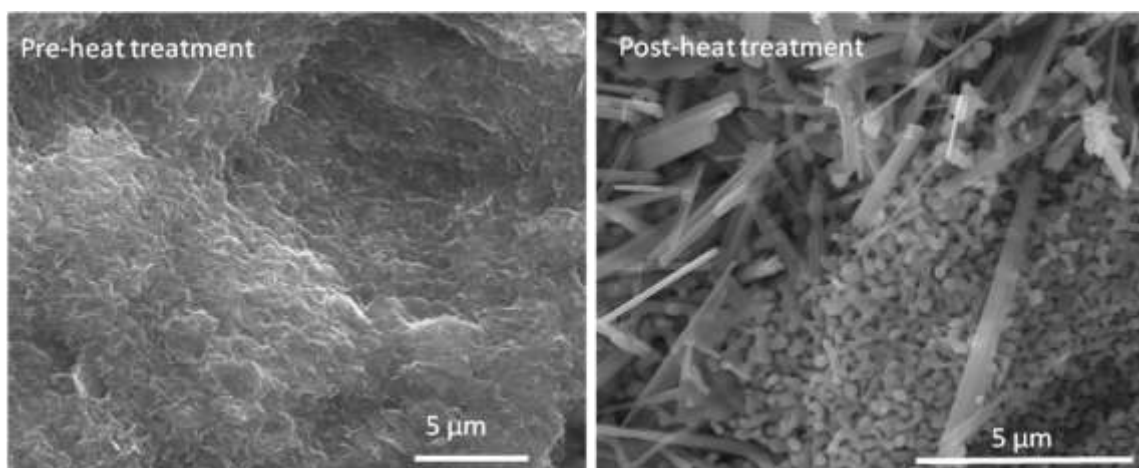


Figure 28. Growth of $\alpha\text{-MnO}_2$ in an Mn_2O_3 matrix from Na -flocculated nanosheets shown before and after heat treatment at $800\text{ }^\circ\text{C}$ for 12 hours.

Using EDS, it can be shown that Na is present only in the tubes shown in Figure 28 and not the regions of Mn_2O_3 . In conjunction with results of H -flocculated MnO_2 that does not show α -phase growth at high temperatures (Figure 25), it is likely that the presence of Na^+ stabilizes $\alpha\text{-MnO}_2$ and encourages its growth during heating.

H. Mechanism of Phase Transformations

The formation of α - MnO_2 and Mn_2O_3 has been theorized to be related to the interlayer defect octahedra that protrude from the sheet surface. The inter-sheet linking mechanism has been proposed based on the defect model put forth by Manceau, et al.,³¹ in conjunction with the out-of-plane manganese observed using PDF measurements. Computational models produced by Li, et al.,⁶² show that these surface-coordinated manganese octahedra can become mobile. Through a stochastic surface walking (SSW) mechanism, MnO_6 octahedra on the surface of the sheet link and connect the sheets together to form tunnels. At high temperatures, the mobility of the octahedra is high enough to destroy the layered structure entirely in favor of 1-dimensional tunnels and 3D crystals.

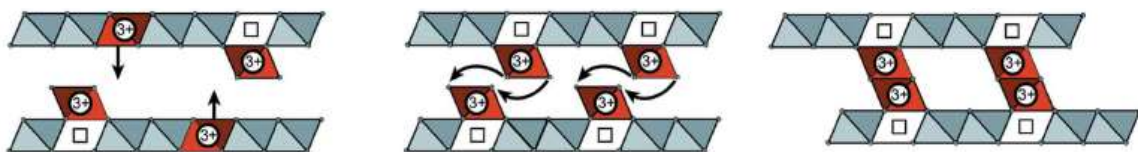


Figure 29. Linking of out-of-plane MnO_6 octahedra to form tunnels.⁶³

Grangeon, et al., found that these surface-mobile MnO_6 octahedra will spontaneously link in the interlayer when their hydration spheres begin to interact, given time for the octahedra to walk across the sheet surface or for the sheets to align.⁶³ It was found through the present work, however, that the mobility of the octahedra can be increased significantly through thermal means, allowing tunnels to form over a matter of minutes. PDF studies found indications of α - MnO_2 formation in pH 2 flocculated δ - MnO_2 at temperatures as low as 200 °C, although this phase is not visible in lab-scale x-ray experiments. From the TGA results shown in Figure 11 and the HTXRD performed on parent-phase and washed birnessites (Figure 9 and Figure 23) show a dehydration of the interlayer occurring above 150 °C accompanied with a decrease in interlayer spacing. It is likely that this shrinking, along with the mobility of surface octahedra, encourages interactions between sheets and allows for the growth of α - MnO_2 .

SUMMARY AND CONCLUSIONS

Nanosheets derived from the exfoliation of bulk layered oxides present a facile method of fabricating both homogeneous films and high surface area, high porosity monoliths for use in applications such as catalysis, filtration, among others. Flocculation provides a direct route to nanoscale self-assembly of sheets into mesoporous solids or even composites that can be further processed into working advanced materials.

Due to the natural prevalence of birnessite in Earth's oceans and soil, much work has been done on natural and synthetic manganese compounds. The natural abundance of manganese oxides and their low toxicity make them ideal materials for commercial use. However, these materials, produced by hydrothermal or aqueous methods, represent highly defective crystals. Through this work, crystals of higher purity were synthesized and investigated to determine the effects of processing on defect content and the role of defects in high-temperature phase stability.

It was found possible to introduce defects to high-quality crystals of MnO_2 through treatment with HCl both before and after exfoliation. These defects play a role in the electrochemical performance of electrodes formed from MnO_2 nanosheets⁵⁶ and also affect the high-temperature phase stability. Through different ion-exchange and flocculation conditions, it is possible to control the final phase composition after heat treatment. High-energy XRD shows the onset of tunnel-structure growth in flocculated sheets as low as 200 °C, while still maintaining the open porous sheet network. At 600 °C, Mn_2O_3 begins to form, changing the microstructure, but maintaining an open pore network.

The conversion of MnO_2 to Mn_2O_3 is not necessarily a detrimental process. The fact that the open pore structure is maintained throughout all of the microstructural and phase changes is very important for proposed applications in catalysis and electrochemical capacitors. Maintaining the high surface area ensures a high density of available sites for catalytic reactions and ionic/molecular surface associations.

FUTURE WORK

The nature of this work lends itself to further experiments beyond the scope of this one project. Several questions reveal themselves from the results found here.

- What exactly does the interlayer look like?
- Is it possible to reliably control the end microstructure through careful pH and heat treatment?
- What applications are possible by flocculating MnO₂ nanosheets with different ions or with different co-flocculating media?

The interlayer of layered systems has garnered great interest due to its high ionic mobility. This work has shown that it is possible to synthesize high-quality crystals with varying interlayer potassium content with little change to the structure. How does the change in potassium content affect the location of these ions in the interlayer, and does that affect how readily they exchange with other ions? This is an interesting problem to consider that may have ramifications on the steps taken to ensure complete replacement of potassium during the ion exchange process in preparation for further processing.

This work and others have shown that the δ polymorph of MnO₂ can be used as an intermediate phase to many manganese oxide polymorphs. Can the control of defect content, as suggested by this work and work built off of samples similarly prepared, allow for specific tailoring of final phase compositions? It may be possible to control the growth of α -MnO₂, for example, through careful heat treatments, although that was not achieved here.

One of the many applications of MnO₂ is as a photocatalyst, and it has been reported to be able to separate water into H₂ and O₂. Can the addition of other photoactive materials within a nanocomposite, such as TiO₂, allow for coupled or synergistic effects to improve hydrogen yield and make fuel cells more viable? This work reported the ability to trap TiO₂ in flocculated nanosheets, but the applications of such a composite were not tested and may prove to have many desirable properties.

REFERENCES

1. K. S. Novoselov, V. I. Fal'ko, L. Colombo, P. R. Gellert, M. G. Schwab, and K. Kim, "A Roadmap for Graphene," *Nature*, **490** 192-200 (2012).
2. L. Wang and T. Sasaki, "Titanium Oxide Nanosheets: Graphene Analogues with Versatile Functionalities," *Chem. Rev.*, **114** [19] 9455-86 (2014).
3. T. Sasaki, "Fabrication of Nanostructured Functional Materials Using Exfoliated Nanosheets as a Building Block," *J. Ceram. Soc. Jpn.*, **115** [1] 9-16 (2007).
4. G. H. Du, Y. Yu, Q. Chen, R. H. Wang, W. Zhou, and L. M. Peng, "Exfoliating KTiNbO_5 Particles into Nanosheets," *Chem. Phys. Lett.*, **377** [3-4] 445-8 (2003).
5. T. Gubb, "Colloidal Processing and Photocatalytic Properties of Titanate-Niobate Nanosheets"; M.S. Thesis. Alfred University, 2016.
6. V. L. Blair, E. J. Nichols, J. Liu, and S. T. Misture, "Surface Modification of Nanosheet Oxide Photocatalysts," *Appl. Surf. Sci.*, **268** 410-5 (2013).
7. K. Fukuda, Y. Ebina, T. Shibata, T. Aizawa, I. Nakai, and T. Sasaki, "Unusual Crystallization Behaviors of Anatase Nanocrystallites from a Molecularly Thin Titania Nanosheet and Its Stacked Forms: Increase in Nucleation Temperature and Oriented Growth," *J. Am. Chem. Soc.*, **129** 202-9 (2007).
8. R. Ma and T. Sasaki, "Two-Dimensional Oxide and Hydroxide Nanosheets: Controllable High-Quality Exfoliation, Molecular Assembly, and Exploration of Functionality," *Acc. Chem. Res.*, **48** [1] 136-43 (2015).
9. M. Ohwada, K. Kimoto, T. Mizoguchi, Y. Ebina, and T. Sasaki, "Atomic Structure of Titania Nanosheet with Vacancies," *Sci. Rep.*, **3** 2801 (2013).
10. B. W. Li, M. Osada, Y. Ebina, K. Akatsuka, K. Fukuda, and T. Sasaki, "High Thermal Robustness of Molecularly Thin Perovskite Nanosheets and Implications for Superior Dielectric Properties," *ACS Nano*, **8** [6] 5449-60 (2014).
11. M. Osada, S. Yoguchi, M. Itose, B. W. Li, Y. Ebina, K. Fukuda, Y. Kotani, K. Ono, S. Ueda, and T. Sasaki, "Controlled Doping of Semiconducting Titania Nanosheets for Tailored Spinelectronic Materials," *Nanoscale*, **6** [23] 14227-36 (2014).
12. P. Sun, R. Ma, K. Wang, M. Zhong, J. Wei, D. Wu, T. Sasaki, and H. Zhu, "Suppression of the Coffee-Ring Effect by Self-Assembling Graphene Oxide and Monolayer Titania," *Nanotechnology*, **24** (2013).

13. X. Cai, R. Ma, T. C. Ozawa, N. Sakai, A. Funatsu, and T. Sasaki, "Superlattice Assembly of Graphene Oxide (GO) and Titania Nanosheets: Fabrication, in Situ Photocatalytic Reduction of GO and Highly Improved Carrier Transport," *Nanoscale*, **6** [23] 14419-27 (2014).
14. M. Liu, Y. Ishida, Y. Ebina, T. Sasaki, and T. Aida, "Photolatently Modulable Hydrogels Using Unilamellar Titania Nanosheets as Photocatalytic Crosslinkers," *Nat. Commun.*, **4** 2029 (2013).
15. K. Taira, Y. Hirose, S. Nakao, N. Yamada, T. Kogure, T. Shibata, T. Sasaki, and T. Hasegawa, "Lateral Solid-Phase Epitaxy of Oxide Thin Films on Glass Substrate Seeded with Oxide Nanosheets," *ACS Nano*, **8** [6] 6145-50 (2014).
16. "Grid Energy Storage," United States Department of Energy, December, 2013.
17. V. Etacheri, R. Marom, R. Elazari, G. Salitra, and D. Aurbach, "Challenges in the Development of Advanced Li-Ion Batteries: A Review," *Energy Environ. Sci.*, **4** [9] 3243-62 (2011).
18. B. Zhao, R. Ran, X. Wu, and D. Weng, "Phase Structures, Morphologies, and NO Catalytic Oxidation Activities of Single-Phase MnO₂ Catalysts," *Appl. Catal. A*, **514** 24-34 (2016).
19. Y. Omomo, T. Sasaki, L. Wang, and M. Watanabe, "Redoxable Nanosheet Crystallites of MnO₂ Derived Via Delamination of a Layered Manganese Oxide," *J. Am. Chem. Soc.*, **125** 3568-75 (2003).
20. R. M. McKenzie, "The Synthesis of Birnessite, Cryptomelane, and Some Other Oxides and Hydroxides of Manganese," *Mineral. Mag.*, **38** 493-502 (1971).
21. A.-C. Gaillot, V. A. Drits, A. Manceau, and B. Lanson, "Structure of the Synthetic K-Rich Phyllosulfate Birnessite Obtained by High-Temperature Decomposition of KMnO₄," *Microporous Mesoporous Mater.*, **98** [1-3] 267-82 (2007).
22. S. H. Kim, S. J. Kim, and S. M. Oh, "Preparation of Layered MnO₂ Via Thermal Decomposition of KMnO₄ and Its Electrochemical Characterizations," *Chem. Mater.*, **11** 557-63 (1999).
23. L. Liu, Y. Luo, W. Tan, Y. Zhang, F. Liu, and G. Qiu, "Facile Synthesis of Birnessite-Type Manganese Oxide Nanoparticles as Supercapacitor Electrode Materials," *J. Colloid Interface Sci.*, **482** 183-92 (2016).

24. M. A. Cheney, R. Jose, A. Banerjee, P. K. Bhowmik, S. Qian, and J. M. Okoh, "Synthesis and Characterization of Birnessite and Cryptomelane Nanostructures in Presence of Hoffmeister Anions," *J. Nanomater.*, **2009** 1-8 (2009).
25. R. Ma, Y. Bando, L. Zhang, and T. Sasaki, "Layered MnO₂ Nanobelts: Hydrothermal Synthesis and Electrochemical Measurements," *Adv. Mater.*, **16** [11] 918-22 (2004).
26. Z. Liu, R. Ma, Y. Ebina, K. Takada, and T. Sasaki, "Synthesis and Delamination of Layered Manganese Oxide Nanobelts," *Chem. Mater.*, **19** 6504-12 (2007).
27. J. E. Post, "Manganese Oxide Minerals: Crystal Structures and Economic and Environmental Significance," *Proc. Natl. Acad. Sci. USA*, **96** 3447-54 (1999).
28. T. A. Mellin and G. Lei, "Stabilization of 10Å-Manganates by Interlayer Cations and Hydrothermal Treatment: Implications for the Mineralogy of Marine Manganese Concretions," *Mar. Geol.*, **115** 67-83 (1993).
29. D. C. Golden, J. B. Dixon, and C. C. Chen, "Ion Exchange, Thermal Transformations, and Oxidizing Properties of Birnessite," *Clays and Clay Miner.*, **34** [5] 511-20 (1986).
30. X. Yang, W. Tang, Q. Feng, and K. Ooi, "Single Crystal Growth of Birnessite- and Hollandite-Type Manganese Oxides by a Flux Method," *Cryst. Growth Des.*, **3** [3] 409-15 (2003).
31. A. Manceau, M. A. Marcus, S. Grangeon, M. Lanson, B. Lanson, A. C. Gaillot, S. Skanthakumar, and L. Soderholm, "Short-Range and Long-Range Order of Phyllosulfate Nanoparticles Determined Using High-Energy X-Ray Scattering," *J. Appl. Crystallogr.*, **46** [1] 193-209 (2013).
32. J. Santillán, S.-H. Shim, G. Shen, and V. B. Prakapenka, "High-Pressure Phase Transition in Mn₂O₃: Application for the Crystal Structure and Preferred Orientation of the CaIrO₃ Type," *Geophys. Res. Lett.*, **33** [15] (2006).
33. E. A. Johnson and J. E. Post, "Water in the Interlayer Region of Birnessite: Importance in Cation Exchange and Structural Stability," *Am. Mineral.*, **91** [4] 609-18 (2006).
34. K. P. Lucht and J. L. Mendoza-Cortes, "Birnessite: A Layered Manganese Oxide to Capture Sunlight for Water-Splitting Catalysis," *J. Phys. Chem. C*, **119** [40] 22838-46 (2015).
35. C. L. Lopano, P. J. Heaney, J. Z. Bandstra, J. E. Post, and S. L. Brantley, "Kinetic Analysis of Cation Exchange in Birnessite Using Time-Resolved Synchrotron X-Ray Diffraction," *Geochim. Cosmochim. Acta*, **75** [14] 3973-81 (2011).

36. J. E. Greedan, N. P. Raju, A. S. Wills, C. Morin, and S. M. Shaw, "Structure and Magnetism in λ -MnO₂. Geometric Frustration in a Defect Spinel," *Chem. Mater.*, **10** 3058-67 (1998).
37. Q. Feng, H. Kanoh, Y. Miyai, and K. Ooi, "Hydrothermal Synthesis of Lithium and Sodium Manganese Oxides and Their Metal Ion Extraction/Insertion Reactions," *Chem. Mater.*, **7** 1226-32 (1995).
38. R. N. DeGuzman, Y. F. Shen, E. J. Neth, S. L. Suib, C. L. O'Young, S. Levine, and J. M. Newsam, "Synthesis and Characterization of Octahedral Molecular Sieves (OMS-2) Having the Hollandite Structure," *Chem. Mater.*, **6** 815-21 (1994).
39. J. Luo, Q. Zhang, A. Huang, O. Giraldo, and S. L. Suib, "Double-Aging Method for Preparation of Stabilized Na-Buserite and Transformations to Todorokites Incorporated with Various Metals," *Inorg. Chem.*, **38** [6106-6113] (1999).
40. Y. C. Zhao, S. Li, and C. A. Wang, "Phase and Morphology Evolution of Manganese Oxides During Thermal Treatment," *Key Eng. Mater.*, **697** 322-6 (2016).
41. F. Geng, R. Ma, Y. Ebina, Y. Yamauchi, N. Miyamoto, and T. Sasaki, "Gigantic Swelling of Inorganic Layered Materials: A Bridge to Molecularly Thin Two-Dimensional Nanosheets," *J. Am. Chem. Soc.*, **136** [14] 5491-500 (2014).
42. F. Geng, R. Ma, A. Nakamura, K. Akatsuka, Y. Ebina, Y. Yamauchi, N. Miyamoto, Y. Tateyama, and T. Sasaki, "Unusually Stable ~100-Fold Reversible and Instantaneous Swelling of Inorganic Layered Materials," *Nat. Commun.*, **4** 1632 (2013).
43. F. Geng, R. Ma, Y. Yamauchi, and T. Sasaki, "Tetrabutylphosphonium Ions as a New Swelling/Delamination Agent for Layered Compounds," *Chem. Commun. (Cambridge, U. K.)*, **50** [69] 9977-80 (2014).
44. Z. H. Liu, K. Ooi, H. Kanoh, W. P. Tang, and T. Tomida, "Swelling and Delamination Behaviors of Birnessite-Type Manganese Oxide by Intercalation of Tetraalkylammonium Ions," *Langmuir*, **16** 4154-64 (2000).
45. Z. Sun, T. Liao, Y. Dou, S. M. Hwang, M. S. Park, L. Jiang, J. H. Kim, and S. X. Dou, "Generalized Self-Assembly of Scalable Two-Dimensional Transition Metal Oxide Nanosheets," *Nat. Commun.*, **5** 3813 (2014).
46. M. S. Song, K. M. Lee, Y. R. Lee, I. Y. Kim, T. W. Kim, J. L. Gunjekar, and S. J. Hwang, "Porously Assembled 2d Nanosheets of Alkali Metal Manganese Oxides

- with Highly Reversible Pseudocapacitance Behaviors," *J. Phys. Chem.*, **114** 22134-40 (2010).
47. A. C. Thenuwara, S. L. Shumlas, N. H. Attanayake, E. B. Cerkez, I. G. McKendry, L. Frazer, E. Borguet, Q. Kang, M. J. Zdilla, J. Sun, and D. R. Strongin, "Copper-Intercalated Birnessite as a Water Oxidation Catalyst," *Langmuir*, **31** [46] 12807-13 (2015).
 48. B. J. Deibert, J. Zhang, P. F. Smith, K. W. Chapman, S. Rangan, D. Banerjee, K. Tan, H. Wang, N. Pasquale, F. Chen, K. B. Lee, G. C. Dismukes, Y. J. Chabal, and J. Li, "Surface and Structural Investigation of a MnO_x Birnessite-Type Water Oxidation Catalyst Formed under Photocatalytic Conditions," *Chem. - Eur. J.*, **21** [40] 14218-28 (2015).
 49. A. Iyer, J. Del-Pilar, C. K. King'ondeu, E. Kissel, H. F. Garces, H. Huang, A. M. El-Sawy, P. K. Dutta, and S. L. Suib, "Water Oxidation Catalysis Using Amorphous Manganese Oxides, Octahedral Molecular Sieves (OMS-2), and Octahedral Layered (OL-1) Manganese Oxide Structures," *J. Phys. Chem. C*, **116** [10] 6474-83 (2012).
 50. A. Boisset, L. Athouël, J. Jacquemin, P. Porion, T. Brousse, and M. Anouti, "Comparative Performances of Birnessite and Cryptomelane MnO₂ as Electrode Material in Neutral Aqueous Lithium Salt for Supercapacitor Application," *J. Phys. Chem. C*, **117** [15] 7408-22 (2013).
 51. W. Du, X. Xu, D. Zhang, Q. Lu, and F. Gao, "Green Synthesis of MnO_x Nanostructures and Studies of Their Supercapacitor Performance," *Sci. China: Chem.*, **58** [4] 627-33 (2015).
 52. X. Dong, W. Shen, J. Gu, L. Xiong, Y. Zhu, H. Li, and J. Shi, "MnO₂-Embedded-in-Mesoporous-Carbon-Wall Structure for Use as Electrochemical Capacitors," *J. Phys. Chem. B*, **110** 6015-9 (2006).
 53. S. L. Suib, "Porous Manganese Oxide Octahedral Molecular Sieves and Octahedral Layered Materials," *Acc. Chem. Res.*, **41** [4] 479-87 (2008).
 54. M. Y. Menetrez, D. G. Anderson, and E. P. Stahel, "Manganese Dioxide Coated Filters for Removing Radium from Drinking Water," United States Environmental Protection Agency, 1989.
 55. C. C. Chen, D. C. Golden, and J. B. Dixon, "Transformation of Synthetic Birnessite to Cryptomelane: An Electron Microscopy Study," *Clays and Clay Miner.*, **34** [5] 565-71 (1986).

56. P. Gao, P. Metz, T. Hey, Y. Gong, D. Liu, D. Edwards, J. Howe, R. Huang, and S. Misture, "The Critical Role of Point Defects in Improving the Specific Capacitance of δ -MnO₂ Nanosheets," *Nat. Commun.*, (In Press).
57. R. Chen, P. Zavalij, and M. S. Whittingham, "Hydrothermal Synthesis and Characterization of K_xMnO₂•yH₂O," *Chem. Mater.*, **8** 1275-80 (1996).
58. T. Takei, Q. Dong, Y. Yonesaki, N. Kumada, and N. Kinomura, "Synthesis and Electronic Structure of Proton-Type Partially Substituted Birnessite by Period-Four Transition Metal," *Mater. Res. Bull.*, **46** [11] 1896-901 (2011).
59. B. Lee, C. S. Yoon, H. R. Lee, K. Y. Chung, B. W. Cho, and S. H. Oh, "Electrochemically-Induced Reversible Transition from the Tunneled to Layered Polymorphs of Manganese Dioxide," *Sci. Rep.*, **4** 6066 (2014).
60. K. S. W. Sing, "Reporting Physisorption Data for Gas/Solid Systems," *Pure & Appl. Chem.*, **54** [11] 2201-18 (1982).
61. P. Metz, 2016, Private Communication.
62. Y. F. Li, S. C. Zhu, and Z. P. Liu, "Reaction Network of Layer-to-Tunnel Transition of MnO₂," *J. Am. Chem. Soc.*, **138** [16] 5371-9 (2016).
63. S. Grangeon, B. Lanson, and M. Lanson, "Solid-State Transformation of Nanocrystalline Phyllo-manganate into Tectomanganate: Influence of Initial Layer and Interlayer Structure," *Acta Crystallogr., Sect. B: Struct. Sci. Cryst. Eng. Mater.*, **70** [Pt 5] 828-38 (2014).